Department of Earth and Environmental Sciences
Macquarie University, NSW 2109, Australia
Phone +61 (0)4 77300674
Email maria-constanza.manassero@mq.edu.au

November 15th , 2022

We present an original manuscript entitled "Lithospheric structure and melting processes in southeast Australia: new constraints from joint probabilistic inversions of 3D magnetotelluric and seismic data" by M.C. Manassero[1], S. Özaydin[1,2], J. C. Afonso[3,4,1], J. Shea[1,5], A. Kirkby[6,7], I. Ezad[1], S. Thiel[8,9] , I. Fomin[1] and K. Czarnota[7].

This paper is a non-peer reviewed preprint submitted to EarthArXiv. The preprint is going to be submitted for peer review to Journal of Geophysical Research: Solid Earth on 23th January, 2023.

Yours Sincerely,

Maria Constanza Manassero* (maria-constanza.manassero@mq.edu.au)
Sinan Özaydin (sinan.ozaydin@mq.edu.au)
Juan Carlos Afonso (j.c.afonso@utwente.nl)
Joshua Shea (Joshua.shea1@hdr.mq.edu.au)
Alison Kirkby (alkirkby@gmail.com)
Isra Ezad (isra.ezad@mq.edu.au)
Stephan Thiel (Stephan.Thiel@sa.gov.au)
Ilya Fomin (ilya.fomin@mq.edu.au)
and Karol Czarnota.

[1] School of Natural Sciences, Macquarie University, Sydney, Australia.
[2] School of Geosciences, University of Sydney, Sydney, Australia
[3] Faculty of Geo-Information Science and Earth Observation (ITC), University of Twente, Enschede, Netherlands
[4] Department of Earth and Space Sciences, Southern University of Science and Technology Shenzhen, Guangdong, China
[5] Department of Materials, The University of Manchester, Manchester M13 9PL, United Kingdom
[6] GNS Science, Wairakei Research Centre, Taupo, New Zealand
[7] Geoscience Australia, Canberra, ACT, 2601, Australia.
[8] Department of Earth Sciences, University of Adelaide, Adelaide, SA 5005, Australia
[9] Geological Survey of South Australia, Adelaide, SA 5001, Australia

*Corresponding author
Australian Research Council Centre of Excellence for Core to Crust Fluid System (CCFS)
Department of Earth and Environmental Sciences, Macquarie University, Sydney, NSW 2109 , Australia
email: maria-constanza.manassero@mq.edu.au

Lithospheric structure and melting processes in southeast Australia: new constraints from joint probabilistic inversions of 3D magnetotelluric and seismic data

M.C. Manassero[1], S. Özaydın[2,1], J.C. Afonso[3,4,1], J. Shea[5,1], A. Kirkby[6,7], I.S. Ezad [1], S. Thiel [8,9], I. Fomin[1] and K. Czarnota[7]

[1]School of Natural Sciences, Macquarie University, Sydney, Australia
[2]School of Geosciences, University of Sydney, Sydney, Australia
[3]Faculty of Geo-Information Science and Earth Observation (ITC), University of Twente, Enschede, Netherlands
[4]Department of Earth and Space Sciences, Southern University of Science and Technology Shenzhen, Guangdong, China
[5]Department of Materials, The University of Manchester, Manchester M13 9PL, United Kingdom
[6]GNS Science, Wairakei Research Centre, Taupo, New Zealand
[7]Geoscience Australia, Canberra, ACT, 2601, Australia
[8]Department of Earth Sciences, University of Adelaide, Adelaide, SA 5005, Australia
[9]Geological Survey of South Australia, Adelaide, SA 5001, Australia

Key Points:

- We apply a novel approach for joint probabilistic inversions of 3D magnetotelluric and seismic data.
- We use the new method to image the lithosphere-asthenosphere system beneath southeastern of Australia.
- The imaged lithosphere correlates with the location of volcanic centers and provides insights on the melt production in the region.

Corresponding author: Maria Constanza Manassero, maria-constanza.manassero@mq.edu.au

Abstract

The thermochemical structure of the lithosphere exerts control on melting mechanisms in the mantle as well as the location of volcanism and ore deposits. Imaging the complex interactions between the lithosphere and asthenospheric mantle requires the joint inversion of multiple data sets and their uncertainties. In particular, the combination of seismic velocity and electrical conductivity with data proxies for bulk composition and elusive minor phases is a crucial step towards fully understanding large-scale lithospheric structure and melting. We apply a novel probabilistic approach for joint inversions of 3D magnetotelluric and seismic data to image the lithosphere beneath southeast Australia. Results show a highly heterogeneous lithospheric structure with deep conductivity anomalies that correlate with the location of Cenozoic volcanism. In regions where the conductivities have been at odds with sub-lithospheric temperatures and seismic velocities, we observe that the joint inversion provides conductivity values consistent with other observations. The results reveal a strong relationship between metasomatized regions in the mantle and i) the limits of geological provinces in the crust, which elucidates the subduction-accretion process in the region; ii) distribution of leucitite and basaltic magmatism; iii) independent geochemical data, and iv) a series of lithospheric steps which constitute areas prone to generating small-scale instabilities in the asthenosphere. This scenario suggests that shear-driven upwelling and edge-driven convection are the dominant melting mechanisms in eastern Australia rather than mantle plume activity, as conventionally conceived. Our study offers an integrated lithospheric model for southeastern Australia and provides insights into the feedback mechanism driving surface processes.

Plain Language Summary

The lithosphere is the outermost rigid layer of the Earth and the focus of important geological processes such as earthquakes (seismic activity), volcanism, and mineralization. The location of these processes often coincide with deep discontinuities in the lithospheric structure. Imaging the structure of the lithosphere using geophysical techniques is then crucial to fully understand the nature of these processes. Obtaining the most reliable images of the lithospheric structure requires the joint analysis of two or more geophysical data sets. In particular, the combination of magnetotellurics (an electromagnetic technique) and seismic data holds great potential due to their complementary sensitivity to the Earth's properties. Combining a joint analysis with a probabilistic approach help us understand the variability of the lithospheric structure better since they provide a large number of models that can explain the data. Given the good data coverage in southeast Australia, we use a new probabilistic approach for the joint analysis of magnetotelluric and seismic data to image the lithosphere structure beneath this region. Our results show a complex lithospheric structure in line with the location of volcanism and tectonic history of the region. Lithospheric composition derived from the models provides significant insights into melt production in the area.

1 Introduction

The magnetotelluric method (MT) has great potential for investigating metasomatism and tectono-magmatic processes in the lithosphere (e.g., Wannamaker et al., 2008; Comeau et al., 2015; Aivazpourporgou et al., 2015; Wannamaker et al., 2014; Bedrosian, 2016; Kirkby et al., 2020; Blatter et al., 2022; Özaydın & Selway, 2022; Cordell et al., 2022). Due to its sensitivity to fluid and/or melt content, MT is particularly useful for probing the connection between deep melt/fluid pathways and their surface expressions, such as the location of ore deposits (e.g., Griffin et al., 2013; Heinson et al., 2018; Kirkby et al., 2022) and volcanic centers (Wei et al., 2001; Comeau et al., 2015). However, MT is not free of limitations. For instance, MT struggles to delineate deep conductivity structures, especially when they are below shallow conductive features. This is due to the diffusive behaviour of electromagnetic waves and the high sensitivity of MT to conductors (Jones, 1999). The MT method is also ambiguous in discerning the different factors that affect electrical conductivity, such as temperature, water/melt content and composition. Unlocking the full potential of the MT method requires the development of methodologies that can assign meaningful physical interpretations to conductivity anomalies and discriminate between their causes (Selway, 2014).

A widely adopted approach to reduce feature ambiguity is the combination of MT with other geophysical data sets via joint inversions (e.g, Khan et al., 2006; Gallardo & Meju, 2007; Jegen et al., 2009; Moorkamp et al., 2010; Bennington et al., 2015; Afonso, Rawlinson, et al., 2016; Jones et al., 2017; Blatter et al., 2019; Manassero et al., 2021; Liao et al., 2022; Wu et al., 2022). By exploiting the complementary sensitivities of different data sets to the properties of interest, joint inversions minimize the range of acceptable models consistent with the available data and can increase model resolution (e.g. Moorkamp et al., 2007; Afonso et al., 2013a; Afonso, Rawlinson, et al., 2016; Afonso, Moorkamp, & Fullea, 2016). For example, in the case of MT and seismic data, both data sets are sensitive (to different degrees) to the background thermal and compositional structure of the lithosphere. However, only MT is strongly sensitive to minor conductive phases (e.g., hydrous minerals and graphite), hydrogen content or small-scale melt/fluid pathways (Karato, 1990, 2006; Evans, 2012; Yoshino, 2010; Khan, 2016; Selway, 2014; Manassero et al., 2021). In this way, joint MT+seismic inversions hold great potential for improving the resolution of conductivity structures (e.g., Moorkamp et al., 2007, 2010; Gallardo & Meju, 2007), detecting regions of partial melting and fluid pathways in the lithosphere (cf., Selway & O'Donnell, 2019; Evans et al., 2019; García-Yeguas et al., 2017; Bennington et al., 2015), as well as understanding their relationship with the location of ore deposits (e.g., Takam Takougang et al., 2015) and metasomatized lithologies (e.g., Snyder et al., 2014).

In addition to the benefits of joint inversions, valuable information about model uncertainties can be obtained via simulation-based probabilistic approaches (Tarantola, 2005; Rosas-Carbajal et al., 2013; Afonso, Rawlinson, et al., 2016; Manassero et al., 2021). Rather than outputting a single best-fitting model, probabilistic approaches provide a distribution of models and their associated probabilities according to their performance in explaining the observations. Thus, probabilistic inversions naturally address the non-uniqueness problem in geophysics (particularly in MT) and quantify model ambiguity (Tarantola, 2005; Gregory, 2005). However, such probabilistic methods require the evaluation of millions of possible models, each in turn requiring the computation of a forward solution. Consequently, simulation-based probabilistic approaches are limited to problems where fast forward operators are available. In the case of 3D MT inversions, fully probabilistic methods have been infeasible due to the large CPU time required by the associated forward problem (Miensopust et al., 2013). In order to address this limitation, Manassero et al. (2020) developed a novel strategy based on reduced order modelling (referred to as RB+MCMC) that allows obtaining fast and accurate approximations of the forward solution and performing joint probabilistic inversions of 3D MT data with other data sets (Manassero et al., 2021). Potential applications and the efficiency of the method to solve the joint inverse problem of MT and seismic data were demonstrated with whole-lithosphere synthetic examples in our previous paper (Manassero et al., 2021).

In this work, we apply the method of Manassero et al. (2020) and Manassero et al. (2021) to a dense array of collocated MT and seismic data in southeastern Australia. This region is known to have experienced multiple orogenic events that resulted in a complex crustal architecture, but its deep lithospheric roots remain poorly characterized (Rawlinson et al., 2016). It also hosts one of the most voluminous intraplate volcanic provinces on Earth, the Eastern Australian Volcanic Province (Johnson et al., 1989). While half of this volcanism can be linked to a hot mantle plume (e.g., Sutherland et al., 2012; Davies et al., 2015), the melting mechanism responsible for the other half is far less clear (Wellman & McDougall, 1974; Shea et al., 2022). Here we focus on the mapping of whole-lithosphere 3D structures and sub-lithospheric temperature anomalies in order to investigate i) the origin of the intraplate magmatism with no clear plume signatures, ii) the connection between deep melt/fluid pathways and the location of volcanic centers, and iii) how lithospheric structure may have influenced melting generation and transport. Southeastern Australia is also a region with abundant xenolith-derived datasets (cf. Shea et al., 2022, and references therein) that can be used to validate the results from our joint inversion.

2 Geological background

The Tasmanides in southeastern Australia are a complex orogenic system that developed from west to east through repetitive cycles of subduction, accretion and lithospheric deformation along the eastern margin of Gondwana (Glen, 2005, 2013; Champion et al., 2016; Rosenbaum, 2018; Moresi et al., 2014). This region is broadly divided into the Delamerian Orogen in the west (early-Palaeozoic) and the younger (mid-Paleozoic) Lachlan Orogen in the southeast (Figure 1.a). Much of the geological complexity in the area can be explained by a geodynamic model of a micro-continent collision and later development of an orocline, referred to as the Lachlan Orocline model (Cayley, 2011; Cayley & Musgrave, 2015; Moresi et al., 2014; Musgrave, 2015). The major structures described in this model are curved crustal geometries with an eastward rotation (Musgrave, 2015), which have been imaged by gravity, magnetic and potential field data (e.g., Musgrave & Rawlinson, 2010; Nakamura & Milligan, 2015; Nakamura, 2016, see Figure 1.c-d,); ambient noise tomography in the crust (e.g., Young et al., 2013; Pilia et al., 2015, see Figure 7.d) and MT conductivity models (Aivazpourporgou et al., 2015; Kirkby et al., 2020; Heinson et al., 2021). Important first-order information about the lithospheric structure beneath southeast Australia has been obtained from conventional studies, such as ambient noise and teleseismic tomography (Rawlinson et al., 2016; Davies et al., 2015; Young et al., 2013), xenolith thermobarometry (e.g., Lu et al., 2018), thermal modeling (e.g., Tesauro et al., 2020) and a recent 3D conductivity model (Kirkby et al., 2020). This latter 3D conductivity model showed, for the first time, that some of the crustal structures associated with the orocline persist below the Moho, providing new insights about the lithospheric architecture and geodynamic history of the region.

Throughout the late Mesozoic and the entire Cenozoic, eastern Australia was subject to voluminous mafic intraplate volcanism, which formed the extensive Eastern Australian Volcanic Province (EAVP, Johnson et al., 1989; Sutherland et al., 2012; Shea et al., 2022). Several regions across eastern Australia contain recent eruptions; in northeastern Australia, the Kinrara vent contains lavas $\sim$7 ka $\pm$ 2 ka (Cohen et al., 2017), while the Mount Gambier, Newer Volcanics (NV) in southeastern Australia contains lavas $\sim$ 4–7.5 ka (Blackburn et al., 1982; Smith & Prescott, 1987).

The EAVP comprises 67 separate volcanic centers with two dominant volcanic center compositions: basalt and potassic leucitite (Figure 1.b). While basaltic volcanics erupted through thinner lithosphere ($<$ 110 km) along the eastern and south-eastern seaboard, the leucitite volcanic centers lie on thick lithosphere ($>$ 125 km) in central New South Wales and central Victoria (Davies & Rawlinson, 2014; Rawlinson et al., 2017). This leucitite suite represents the most atypical and extraordinarily enriched melt compositions reported for mafic melts in eastern Australia (Cundari, 1973; Birch, 1978). Particularly, they represent melts from pervasively metasomatized source assemblages, likely a Ti-bearing oxide phlogopite websterite $\pm$ apatite (see the recent review by Shea et al., 2022). The lack of anhydrous peridotite and the abundance of hydrous minerals in their mantle source assemblages is of particular importance to this work, indicating widespread mantle metasomatism beneath eastern Australia.

The EAVP is also unique in the sense that about half of the volcanism is age-progressive and commonly linked to a hot mantle plume (e.g., Sutherland et al., 2012; Davies et al., 2015), whereas the remaining volcanic centres show no age-progression and no obvious melting mechanism (Wellman & McDougall, 1974). To further exacerbate this issue, lava compositions throughout the EAVP (including both age-progressive and non-age-progressive volcanic centers) argue for low-temperature melting of metasomatized mantle source lithologies. In contradiction to the presence of a hot mantle plume, these compositions suggest mild, but localized perturbations in mantle temperatures (Shea et al., 2022).

3 Methods and data sets

3.1 Data

The input data used in our joint probabilistic inversion include magnetotelluric (MT) data from the AusLAMP array (Australian Lithospheric Architecture Magnetotelluric Project) in southeast Australia and P-wave velocities from the tomography model of Rawlinson et al. (2016). The long-period MT data were acquired at 298 AusLAMP stations (blue triangles in Figure 1.f) across a ∼55 km spaced array covering an area of 950 × 950 km. Details about the data acquisition and processing are given in Kirkby et al. (2020). The MT data are the full impedance tensor for periods between 6.4 to 40,000s. Error floors are set to 5% of $\max(|Z_{xx}|, |Z_{xy}|)$ for the components Z_{xx} and Z_{xy} and 5% of $\max(|Z_{yy}|, |Z_{yx}|)$ for the components Z_{yy} and Z_{yx}. We assume uncorrelated data errors that follow a double exponential distribution (e.g., Farquharson & Oldenburg (1998); Rosas-Carbajal et al. (2013); Manassero et al. (2021)).

The P-wave velocity model used in this study (Rawlinson et al., 2016) was constructed from teleseismic tomography using data from the mainland component of the WOMBAT transportable seismic array (Rawlinson et al., 2015). In order to account for the unresolved crustal component of the teleseismic arrival time residuals, the model of Rawlinson et al. (2016) includes a detailed crustal model from ambient noise tomography (Young et al., 2013) and the Moho from AuSREM (Kennett & Salmon, 2012) as starting model of the tomographic inversion. Despite this additional constraint, uncertainties in absolute velocities within the crust remain relatively high, especially in the lower-crust (Young et al., 2013; Rawlinson et al., 2016). We obtained seismic velocities by interpolating the velocity model on a data-point grid of 50×50 km at the surface (shown in red dots in Figure 1f) and 24 points between the surface and 340 km depth. The velocity data errors are assumed to be uncorrelated and normally distributed with a standard deviation of 1%, according to Burdick & Lekić (2017). Examples of data and data fits for MT data and seismic velocities are shown in Figures 2. Additional figures can be found in the Supplementary Material.

3.2 Bayesian inversion

In the Bayesian or probabilistic approach to the inverse problem, inference about the model parameters $\mathbf{m}$ given observed data $\mathbf{d}$ is based on the so-called posterior probability density function (PDF):

$$P(\mathbf{m}|\mathbf{d}) = \frac{P(\mathbf{d}|\mathbf{m})P(\mathbf{m})}{P(\mathbf{d})} \propto \mathcal{L}(\mathbf{m})P(\mathbf{m}) \propto exp(\phi)P(\mathbf{m}), \tag{1}$$

where $P(\mathbf{m})$ denotes the prior PDF describing all the information on the model's parameters prior to the inversion (e.g., prior geological or petrological knowledge in the area of study). $\mathcal{L}(\mathbf{m})$ is the likelihood function, which is specified by the statistical distribution of the data errors, and ϕ is the *misfit* of model $\mathbf{m}$. In the case of MT, the data mis-

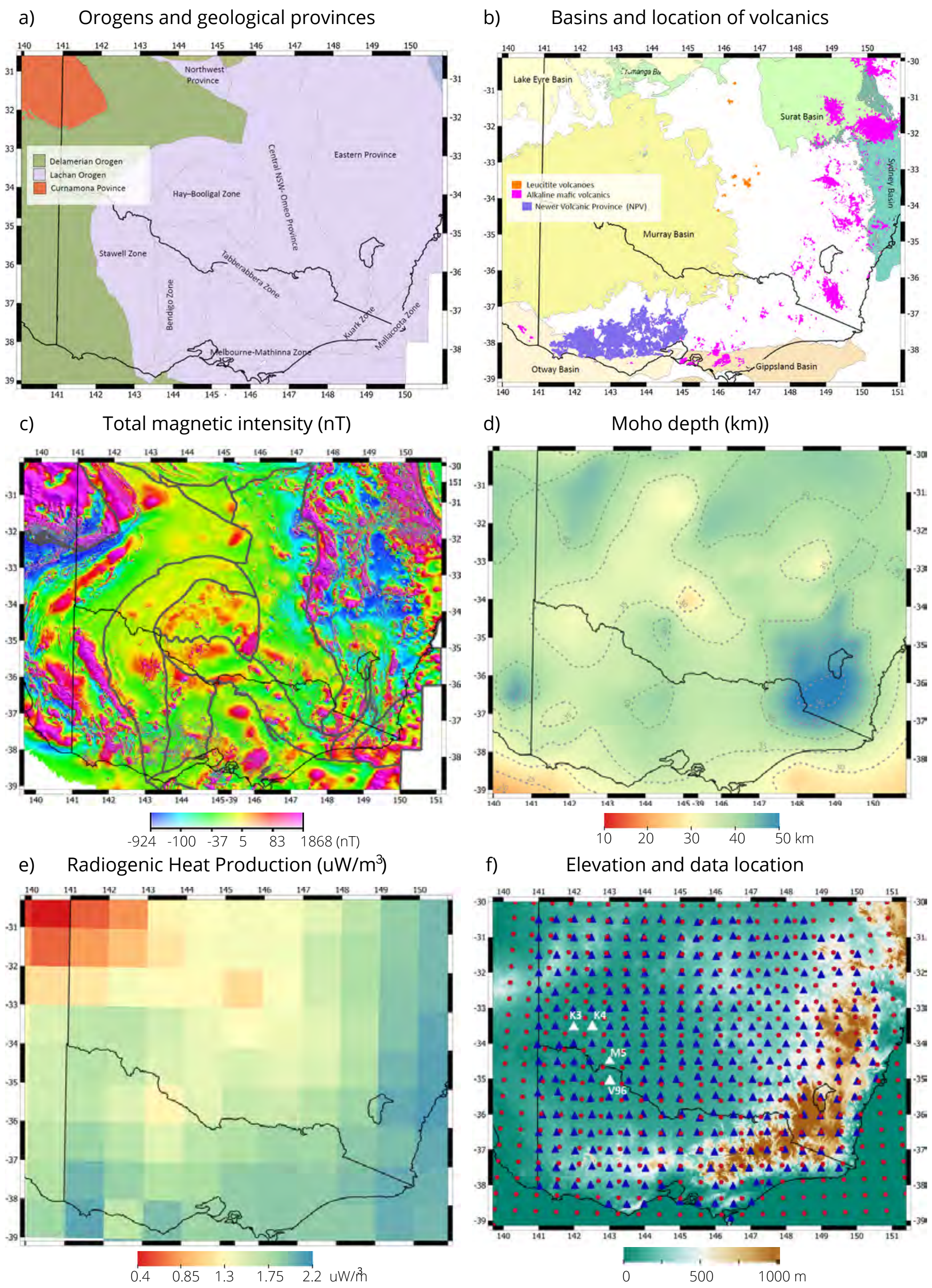

Figure 1. Maps showing (a) orogens that comprise the Tasmanides of southeastern Australia with grey outline denoting geological provinces (Raymond et al., 2018); (b) Mesozoic to Cenozoic sedimentary basins after Raymond et al. (2012), leucitites volcanoes (orange) and basaltic volcanics (pink) after Shea et al. (2022). The basaltic in NV are highlighted in purple. (c) Total magnetic intensity map (TMI) which includes airborne-derived TMI data for onshore and near-offshore continental areas (Nakamura & Milligan, 2015). (d) Moho depth from the AusREM model (Kennett & Salmon, 2012) where 5km-contour lines are shown in dashed-grey. (e) Mean crustal RHP from Haynes et al. (2020) (f) Elevation map of southeast Australia including the AusLAMP MT stations (blue triangles) and the location of the velocity data (red dots). Panel (a) and (c) show major tectonic boundaries are outlined in grey. White triangles indicate stations where data fits are shown.

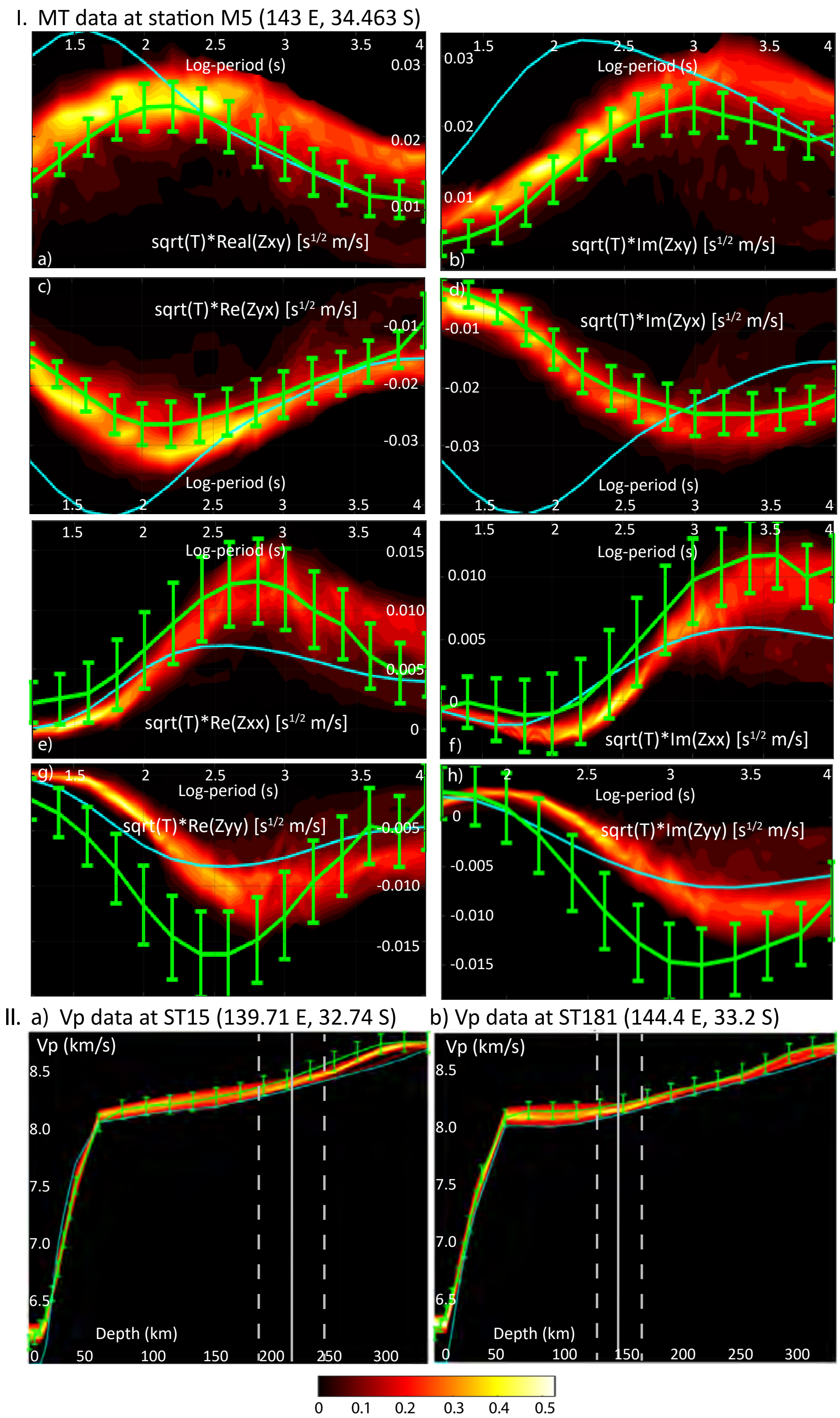

Figure 2. I. Posterior PDFs (refer to next section) of MT data for station M5. Field data and error bars are plotted in green and the computed data for the initial model is plotted in blue. Panels (a), (b), (c) and (d): Posterior PDFs of the real and imaginary parts of the off-diagonal components (Zxy and Zyx). Panels (e), (f), (g) and (h): Posterior PDFs of the real and imaginary parts of the diagonal components (Zxx and Zyy). The data has been scaled by the square-root of the period (T) in all panels. The location of the station is shown in Figure 1f.
II. Posterior PDFs (refer to next section) of P-wave velocity data for stations (a) ST15 located at 139.71 E, 32.74 S and (b) ST182 at 144.4 E, 33.20 S. P-wave velocity data and error bars are plotted in green and the computed data for the initial model is plotted in blue. For those locations, the LAB depths corresponding to the mean, lower and upper bound of the 68% CI models are shown in solid and dashed grey lines, respectively

fit is given by (Tarantola, 2005):

$$\phi = -\sum_{i=1}^{N} \frac{|g_i(\mathbf{m}) - d_i(\mathbf{m})|}{s_i}, \tag{2}$$

whereas the misfit for the seismic data takes the following form:

$$\phi = -\frac{1}{2}\sum_{i=1}^{N} \Big(\frac{g_i(\mathbf{m}) - d_i(\mathbf{m})}{s_i}\Big)^2. \tag{3}$$

For each data set, $\mathbf{g}$ is the solution of a particular forward problem for model $\mathbf{m}$, N is the total number of data and s_i denotes the standard deviation for the *i-th* data error.

The posterior PDF over data and parameters is commonly approximated using sampling-based Markov chain Monte Carlo (MCMC) algorithms (Gilks et al., 1995). In our joint inversions of independent data sets, we use the Delayed Rejection Adaptive Metropolis (DRAM) scheme of Haario et al. (2006) in combination with the Cascaded Metropolis (CM) approach (Tarantola, 2005; Hassani & Renaudin, 2013; Manassero et al., 2021). Details about the general inversion framework (RB+MCMC) are given in Manassero et al. (2021) while particular details about the sampling strategy, prior information, and the initial seismic velocity and electrical conductivity models used for the current inversion are given in Section S1 of the Supplementary Material.

3.3 Model parameters

In order to define the model parameters and their interdependence in the joint inversion, we distinguish between primary and secondary parameters (Khan et al., 2006; Afonso et al., 2013a; Manassero et al., 2021). The latter are directly linked to the properties used to solve the forward problems in their classic forms (e.g., V_p and electrical conductivity). The former are the fundamental thermodynamic parameters, namely, temperature (T), pressure (P) and bulk composition (C). These control the magnitudes of the secondary parameters in the mantle via equations of state and thermodynamic constraints (this applies to the mantle only; for crustal parameters see below). A specific configuration of the primary parameters in the 3D space defines what we refer to as the *background state* (or background contribution). In this way, the background P-wave velocity and electrical conductivity in the mantle can be written as $V_p(T,P,C)$ and $\sigma_b(T,P,C)$.

As shown by Afonso et al. (2013a, 2013b) and Manassero et al. (2021), an efficient way to parameterize the background state is to divide the 3D space into m rectangular columns and use the following model parameters in each column: i) the depth to the thermal lithosphere-astenosphere boundary (LAB), here defined as the $1250°C$ isotherm (Afonso, Moorkamp, & Fullea, 2016), and ii) n 'thermodynamic nodes' distributed throughout the mantle. The LAB depths allow us to solve for a lithospheric conductive temperature profile, while the temperature of the thermodynamic nodes placed in the sub-lithospheric mantle are allowed to vary during the inversion as required by the inverted data. The computation of the pressure (P) and definition of the bulk composition (C) are described below and in Section 3.5, respectively.

Since the electrical conductivity is also highly sensitive to factors other than T, P, and C (e.g., hydrogen content, localized fluid/melt pathways, presence of hydrated phases or graphite), we expand the space of secondary parameters and write $\sigma = \sigma_b(T,P,C) + \sigma(X)$, where X stands for any factor that cannot be captured by the background. This means that $\sigma(X)$ is a representation of any anomalous conductivity associated with processes superimposed on the background state (Manassero et al., 2021). This anomalous conductivity contribution and the conductivity in the crust ($\sigma_c(X)$) are parameterized with l conductivity nodes distributed throughout the whole domain (see details in Section S3 in Supplementary Material and in Manassero et al., 2021).

In order to parameterize the rest of the properties of the crust, we divide the crust into three layers (sediments, upper crust and lower crust) from the surface to the Moho. Within each column, layers have fixed thicknesses and their own set of physical properties: thermal conductivity (k), volumetric radiogenic heat production (RHP) and P-wave (V_p) velocity. During the inversion, only V_p is allow to vary within their assigned uncertainties (Rawlinson et al., 2016); all remaining parameters are assumed constant. The thermal conductivity of the crustal layers are set to k^1=2.8, k^2=2.6 and k^3=2.3 W/m^oC. The crustal RHP is obtained using the mean crustal RHP from a previous 1D joint probabilistic inversion (Figure 1.e Haynes et al., 2020) while the Moho depths are taken from the regional AusREM model (Kennett & Salmon, 2012). We also incorporate one conductivity cell below each MT station as extra parameters to account for the galvanic distortion effect produced by near-surface inhomogeneities beyond the resolution of our model (Jones, 2011; Chave & Jones, 2012; Avdeeva et al., 2015). Similarly to the approach used in ModEM (Kelbert et al., 2014), these cells are placed in the first (thin) layer of the numerical mesh used to solve the MT forward problem.

3.4 Forward Problems and Model Discretization

The main forward problems solved during the probabilistic inversion are the 3D MT problem and the conductive heat transfer in the lithosphere. These have been described in detail in Manassero et al. (2020, 2021) and in Afonso et al. (2013a, 2013b); Afonso, Rawlinson, et al. (2016), respectively. In what follows, we focus on the model discretization and on the derivation of the seismic velocity and background conductivity models given a realization of the primary parameters.

The study area is subdivided into 441 columns of size 0.45°×0.45°×410 km. Each column is discretized at three different scales:

1. The coarser discretization includes the mantle thermodynamic nodes, placed every 50 km in the vertical direction. These nodes are used to obtain stable mineral assemblages and physical properties in the mantle by Gibbs free-energy minimization (Afonso et al., 2013b).
2. The intermediate discretization comprises the finite elements (FE) used to solve the MT forward problem. In each column, we have 3×3×36 FE (a total of $63\times 63 \times 36$ FE in the whole domain) of size 17×17 km in the horizontal and variable vertical size with depth. The air comprises four FE cells and a total thickness of 106 km.
3. A fine mesh (2 km) is used to solve the steady-state heat transfer equation within the lithosphere (via a FE algorithm), subject to Dirichlet boundary conditions at the LAB (T_{LAB} = 1250 ^{o}C) and at the model's surface (T_S = 10 ^{o}C) (Afonso et al., 2013b).

During the probabilistic inversion, a realization of the background parameters includes a specific LAB depth and temperatures for all the sub-lithospheric thermodynamic nodes in the entire domain, both randomly sampled from their prior distributions. After solving for the conductive geotherm corresponding to the sampled LAB depth, we interpolate the temperatures to the lithospheric thermodynamic nodes (i.e. those thermodynamic nodes that reside inside the lithosphere). The pressure is computed at all thermodynamic nodes using a quadratic lithostatic-type approximation (see Section S2 of Supplementary Material). Using these T, P and a pre-defined composition, we retrieve all thermo-physical properties at the thermodynamic nodes from pre-computed tables. These tables are calculated by Gibbs free-energy minimization with components of the software Perple_X (Connolly, 2009; Afonso et al., 2013b) and the database and thermodynamic formalism of Stixrude & Lithgow-Bertelloni (2011), within the CFMAS system ($CaO, FeO, MgO, Al_2O_3, SiO_2$). All thermophysical properties computed at the thermodynamic nodes are linearly interpolated to the fine mesh to create the corresponding seismic model and to the FE mesh for the computation of the conductivity model (see details in Section S2) and the MT forward solution.

3.5 Mantle composition

The pre-computed tables and their equilibrium assemblages are computed using a mean bulk mantle composition (i.e., specific CFMAS compositions) of 44.3 wt% SiO_2, 2.8 wt% Al_2O_3, 8.5 wt% Fe_2O_3, 39.3 wt% MgO and 2.7 wt% CaO. We estimate this mean composition by averaging eight spinel lherzolites xenoliths (see Table S2 in Supplementary material) that were entrained in EAVP lavas. We use major element compositions from Irving (1980), O'Reilly & Griffin (1987), Griffin et al. (1987) and unreported samples from Bokhara River (J. Shea, personal communications), which cover the area of interest. Since this is the most recent volcanism in eastern Australia, these xenoliths are the most representative samples of current mantle compositions available.

The use of an average mantle composition is justified by the fact that V_p and electrical conductivity have second-order sensitivity to (dry) bulk mantle composition (see Figure S1, S2 and Özaydın & Selway, 2020; Trampert et al., 2001; Goes et al., 2000). We also assume a dry mantle composition for the background properties. The reasons for this choice are: i) Vp is not significantly affected by the small amounts of water commonly observed in mantle samples (Yu et al., 2011; Cline Ii et al., 2018, and references therein), and ii) the conductivity nodes can represent any positive anomalies (e.g., water content) over the background values (which represents the most resistive end-member at the given T-P-C conditions), which reduces the number of parameters by two (see Manassero et al., 2021).

3.6 Mantle water content as a proxy for metasomatism

Using outputs of the joint probabilistic inversion (thermal structure, conductivity models, equilibrium assemblages and mineral compositions), we can estimate the bulk water content in the mantle (i.e. hydroxyl or OH^- bound to nominally anhydrous minerals) that would be required to explain the inversion results. Importantly, the water content as estimated here lumps all unmodeled chemical effects resulting in high conductivity (e.g. connected sulfides, presence of melt) and it is taken as a proxy for mantle metasomatism (see Discussion)

The water content computations are done using the software MATE (Özaydın & Selway, 2020), which includes several experimental models for electrical conductivity, water partitioning and solubility (based on petrological studies). In particular, we used the electrical conductivity models of Gardés et al. (2014), Dai & Karato (2009a), Liu et al. (2019), and Dai & Karato (2009b) for olivine, orthopyroxene, clinopyroxene and garnet, respectively.

The solutions for the water content lie between the bounds defined by the dry lithosphere (i.e., 0 ppm) and the maximum bulk water content calculated using the olivine water solubility model of Padrón-Navarta & Hermann (2017). The experimental coefficients used in the water partitioning are: $D^{OH}_{opx/ol} = 5.6$, $D^{OH}_{cpx/opx} = 1.9$ of Demouchy et al. (2017) and $D^{OH}_{gt/ol} = 0.8$ of Novella et al. (2014); which reflect the sub-solidus conditions found in the continental lithospheric mantle in southeastern Australia. Since we aim to portray variations of water content in the mantle rather than fitting the real water content seen in xenoliths, the choice of the experimental parameters is adequate for our calculations. All water calculations are done using the calibration of Withers et al. (2012) for olivine, and the calibration of Bell et al. (1995) for pyroxenes and garnet.

The electrical conductivity of each individual mineral phase is turned into bulk conductivity through the Generalised Archie's Law (Glover, 2010) with cementation components (m) of $m = 2$ for orthopyroxenes, $m = 4$ for clinopyroxenes and garnet, and

$m < 1$ for olivine (perfectly connected). The Generalised Archie's Law is preferred over the conservative estimates of Hashin-Shtrikman lower-bound since it allows us to incorporate the effects of specific minerals in the conductivity values, such as highly-interconnected phlogopites. The main cementation components used here, however, provide similar values to the Hashin-Shtrikman lower-bound for a lherzolitic matrix (Özaydın & Selway, 2020).

4 Results

4.1 Thermal structure of Southeast Australia

The depth to the LAB obtained from the joint probabilistic inversion of seismic velocities and MT data is shown in Figure 3; the complete 3D temperature structure is shown via depth slices in Figure 4 (first three columns). Figure 3 also includes a recent LAB model obtained from a low-resolution 1D joint probabilistic inversion of elevation, surface heat flow, Rayleigh wave dispersion curves, and geoid anomalies (Haynes et al., 2020; Afonso et al., 2013b) and the estimated LAB depths from two recent seismic tomography models in eastern Australia (Davies et al., 2015; Rawlinson et al., 2017). The maximum absolute difference in lithosphere thickness inside the region is $\sim$ 200 km, with shallow LAB depths ($<$ 100 km) in the eastern and southern ends of the continental block and deep LAB depths ($>$ 250 km) beneath the Curnamona Province (CP) and the northern part of the Delamerian Orogen. We observe a clear correlation between lithospheric structure and the locations of recent volcanism (e.g., Figure 3.a): leucitite volcanic centers correlate with regions of intermediate lithospheric thickness (125-160km) while the basaltic volcanoes are located in regions where the LAB is shallower than 120 km. At least two clear and step-like changes in LAB depth are observed in our model along a transect from the CP to the southeast corner of the model and across the leucitite volcanoes (see also Figures 10).

The first order features of our LAB model are in good agreement with the mean LAB obtained by Haynes et al. (2020), even though the data sets used in each inversion are different. Many features in our LAB model are also present in those derived from seismic velocity models (Davies et al., 2015; Rawlinson et al., 2017). In particular, we observe similar LAB depths beneath the basaltic volcanoes and west of 146^{o}E, where a wedge-like structure follows the curvature of the Stawell Zone (SZ, see Figure 3.1). All models show a thickening of the lithosphere towards the northwest part of the region. However, some significant discrepancies are found in the CP and towards the center of the model. Beneath the CP, our LAB depths are considerably larger than those of Davies et al. (2015) and Rawlinson et al. (2017). While one could attribute some of this difference to the fact that the mantle composition in this area is likely more depleted (and thus 'faster') than the average bulk mantle composition used here (see Section 3.5), additional calculations shown in Figure S3.a of the Supplementary Material reject this possibility as the main cause. Rather, the main reason is the different definitions of LAB adopted in these works. While in shallow lithospheric environments there is a marked minimum in V_p near the LAB (and thus easy to pick), deep lithospheric environments are characterized by smooth V_p profiles, which makes it harder to choose the thermal LAB unambiguously (Figures S3.b and 2.II) based on V_p profiles only. This therefore explains why our LAB estimates are similar to those in Davies et al. (2015) and Rawlinson et al. (2017) in thin lithospheric settings, but they diverge in absolute magnitude when the LAB gets thicker.

The depths to the thermal LABs obtained after an RB+MCMC inversion using MT data alone (Figure S5 in Supplementary Material) are shown in Figure S6 (Supplementary Material). Compared to the results from the joint inversion, these figures show large variability and no clear trend in the thickness of the lithosphere from the CP to the southeast corner of the model (a feature observed in all other models). This comparison illustrates well the facts that i) MT alone has difficulties in discriminating thermal causes from other factors controlling the electrical conductivity in the mantle (Jones, 1999) and ii) other types of data (e.g., seismic) need to be included when imaging lithospheric structure.

4.2 Seismic velocity structure

Depth slices of the P-wave velocity structure predicted by our model are shown in Figure 4. The P-wave velocity model of Rawlinson et al. (2016) is also shown for reference. In all cases, the velocities are plotted relative to the AusREM model at $34.4^o S, 145^o E$ (Figure S4 in Supplementary Material). We observe that the inversion succeeded in reproducing the V_p structure of the input model (Rawlinson et al., 2016). In particular, the mean P-wave velocity down to 100 km is practically identical in both models. The Newer Volcanic province stands out as a low-velocity anomaly at depths between 60 and 80 km, whereas the basaltic volcanoes in the middle of the Eastern Province ($\sim 149^o E$, $34^o S$) correlate well with deeper low-velocity anomalies.

Some minor discrepancies between our results and the model of Rawlinson et al. (2016) are observed at depths $>$ 100 km. For instance, we obtain slightly higher seismic velocities (0.6% higher on average) in the depth range 100-180 km at the eastern end of the model. Supplementary tests allows us to attribute these differences to the constraints imposed by the MT in the joint inversion. Similarly, we obtain slightly slower velocities throughout the whole model at 200-220 km depth (see Figure 4). At these depths, the local discrepancies are consequence of the different physical parameterizations used in this work and by Rawlinson et al. (2016). Nevertheless, neither the original tomography model of Rawlinson et al. (2016) nor our model have sufficient resolution at these depths to justify further comparisons.

4.3 Electrical conductivity structure

The conductivity models for the crust and mantle predicted by the joint inversion are shown in Figures 5 and 6, respectively. For comparison, these figures include the results obtained from a recent deterministic inversion of MT data (Kirkby et al., 2020), using the ModEM software (Kelbert et al., 2014). The main structures observed in the conductivity models are comparable (within model uncertainties) to those in the model of Kirkby et al. (2020) at all depths.

4.3.1 Crust

Figure 7 illustrates the agreement between the conductivity structure in the crust and other sources of information: sedimentary basins (Raymond et al., 2012), magnetic anomalies (Nakamura & Milligan, 2015) and a shear velocity model (Pilia et al., 2015). In particular, Panel (a) shows that the extent of the Paleozoic to Cenozoic sedimentary basins in the region is well outlined by the mean conductivity model at 2 km depth. A comparison between Panels (c,e,f) and Panel (b) highlights the correlation between total magnetic anomalies and conductivity features at different depths. Examples of these are (A) a conductor in the CP; (B) a SW-NE linear structure close to the NW limit of Murray Basin; conductors (C) and (D) in the Tabberabbera Zone; (E) a N-S conductor aligned with the western border of the Eastern Province; (F) two resistive structures west of the Sydney Basin; (G) the Sydney Basin; (H) a conductive region aligned with the north limit of the Northwest and Central NSW provinces; (I) a highly resistive region in the Stawell Zone near the NSW-VIC border; (J) a circular structure in the middle of the model; (K) a high-conductivity anomaly; and (L) a conductor east of CP.

The conductor (A) correlates well with the conductor seen in the MT study of Robertson et al. (2016), using data from 74 AusLAMP stations placed in the Ikara–Flinders Ranges

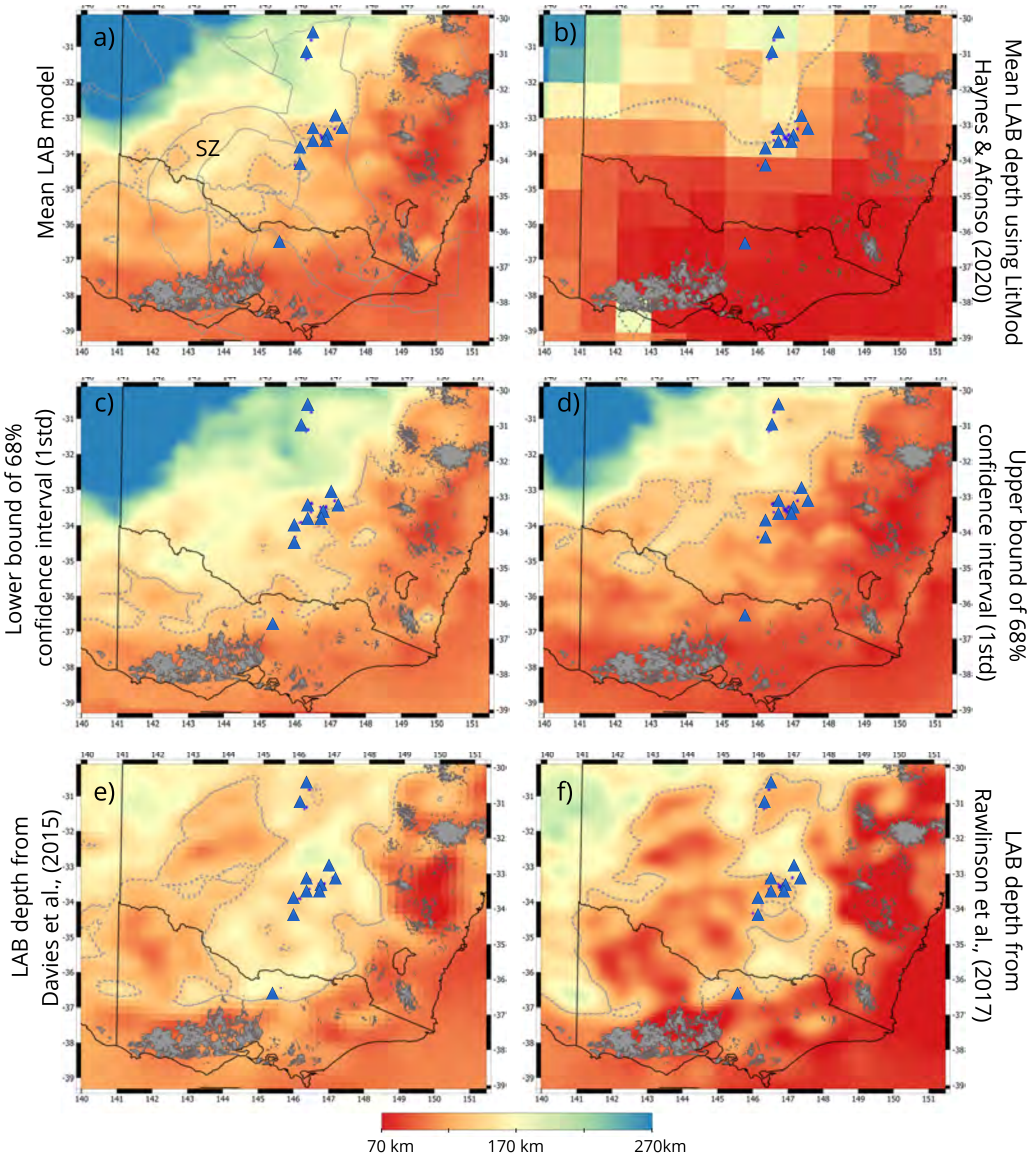

Figure 3. Depth of the thermal LAB. (a) Mean model after the joint probabilistic inversion; (b) mean model obtained after a 1D joint probabilistic inversion (Haynes et al., 2020; Afonso et al., 2013b); (c) and (d) lower and upper bounds of the 68 % confidence interval (1 standard deviation from the mean), respectively. (e) and (f) depth of the LAB after Rawlinson et al. (2017) and Davies et al. (2015), respectively. The location of leucitite-bearing volcanism are shown in blue and standard basaltic volcanoes in grey. The 140 km-contour of the LAB depth in shown in dashed-grey line and the outline of the tectonic provinces in solid grey lines. The location of the Stawell Zone (SZ) is marked in panel (a).

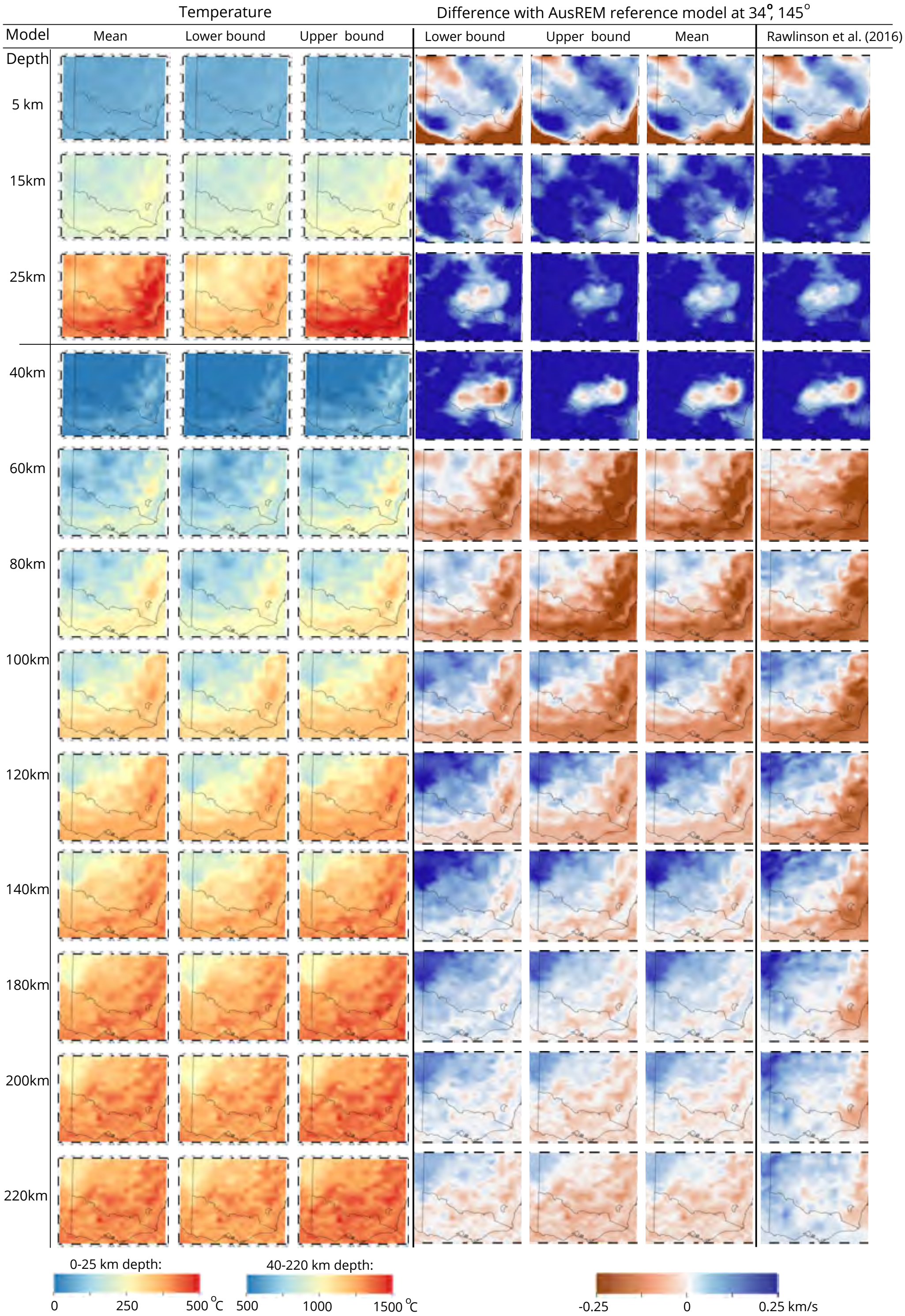

Figure 4. Columns (1)-(3): depth slices from the (1) mean model and those models corresponding to (2) the lower and (3) upper bound of the 68% CI of the posterior PDF for the temperature. Columns (4)-(6): depth slices from the models corresponding to (4) the lower and (5) upper bound of the 68% CI, and (6) mean of the posterior PDF for the P-wave velocity; Column (7): P-wave velocity model of (Rawlinson et al., 2016). Selected depths are shown on the left of the figure. In all cases, velocities are plotted relative to 1-D reference model AusREM at $34.4^o S, 145^o E$ shown in Figure S4 of the Supplementary Material.

and CP, and in the recent study of Kay et al. (2022), using a densely-spaced MT modeling scheme. Comparing Panels (c) and (d), we observe that the main conductivity structures correlates well with velocity anomalies imaged by the shear-wave velocity model of Pilia et al. (2015). We note that the concentric geometries at 29 km depth, such as conductor (J) and structures on the west of the model, resemble the features of the Lachlan Orocline model revealed by potential field and passive seismic data (c.f. Kirkby et al., 2020).

4.3.2 Mantle

The conductivity models between 80-250 km depth (Figures 6) largely resemble the ModEM model of Kirkby et al. (2020). In particular, we observe a similar north-eastward orientation of the conductors in the middle of the model (C_1,C_2,C_3, C_4 and C_5 in Figures 6 and 8). Comparing the mantle conductivity with the mean LAB structure in Figures 8, our models suggest that there is some correlation between the LAB topography and these mantle conductors (cf. Kirkby et al., 2020). In particular, the general NE-SW trend of the conductors tend to follow the LAB depth structure. Conductor C_5 aligns well with the LAB wedge northwest of the model, whereas C_{3N} and C_4S tend to follow the 120-140 km LAB depth iso-surfaces. C_1,C_2 and C_3S are located in regions where LAB depths < 120 km. We also observe an intra-lithosphere high-conductivity structure beneath the CP (C_6), which agrees well with the structure imaged by previous MT studies (e.g., Robertson et al., 2016; Thiel & Heinson, 2013). A high-conductivity region (C_4) is observed below the central-leucitite volcanoes. In our models, the extent of this region is larger and more connected than in the ModEM model.

The main difference between our conductivity model and that of Kirkby et al. (2020) is that the sub-lithospheric conductivities along the south-east coast and in the middle of the region are higher in our model (R_1 and R_2 in Figure 6). The same is true when we compare our model with the results from a probabilistic inversion of MT data only (Figure S5, Supplementary Material). The high resistivity ($> 10^4$ Ωm) values in MT-only inversions are at odds with the mantle resistivity range obtained for sub-lithospheric temperatures and pressures (Fullea et al., 2011; Naif et al., 2021). We observe that, due to the constraint imposed by seismic data in the joint probabilistic inversion (via the thermal structure), unrealistically high resistivity values are not present in our model.

Another example of the constraint imposed by the seismic data in the conductivity models is shown in Figures 8. At 140 km depth, we observe that the conductors in the east (C_1, C_2 and C_{3S} in Figure 8.c) are located within a region defined by a 1250^{o}C-contour (Figure 8.b). These mantle conductivity structures correlate well with both the location of the eastern basaltic volcanics and a stripe of low P-wave seismic velocities (Figure 8.d). At the same time, the stripe of high seismic velocities beneath the east coast at a depth of 140 km is a clear example of the constraint imposed by the MT data in the velocity models. This stripe is not seen in the models of Rawlinson et al. (2016) and correlates with a relatively cold and highly resistive mantle (Figures 8.b-c).

The similarities between the mantle conductivity models at ∼40-80 km depth and features found in the gravity anomalies (Nakamura, 2016) are shown in Figures S7 in the Supplementary Material.

4.4 Joint assessment of bulk water content and temperature maps

The bulk water content maps derived from the mantle conductivity models are shown in Figures 9. As mentioned in Section 3.6, we emphasize that “bulk water content” is a lumped proxy for general mantle metasomatism and therefore their absolute values need to be taken with caution. We observe that most of the localized conductive anomalies above the background require relatively high bulk water contents. This is the case for

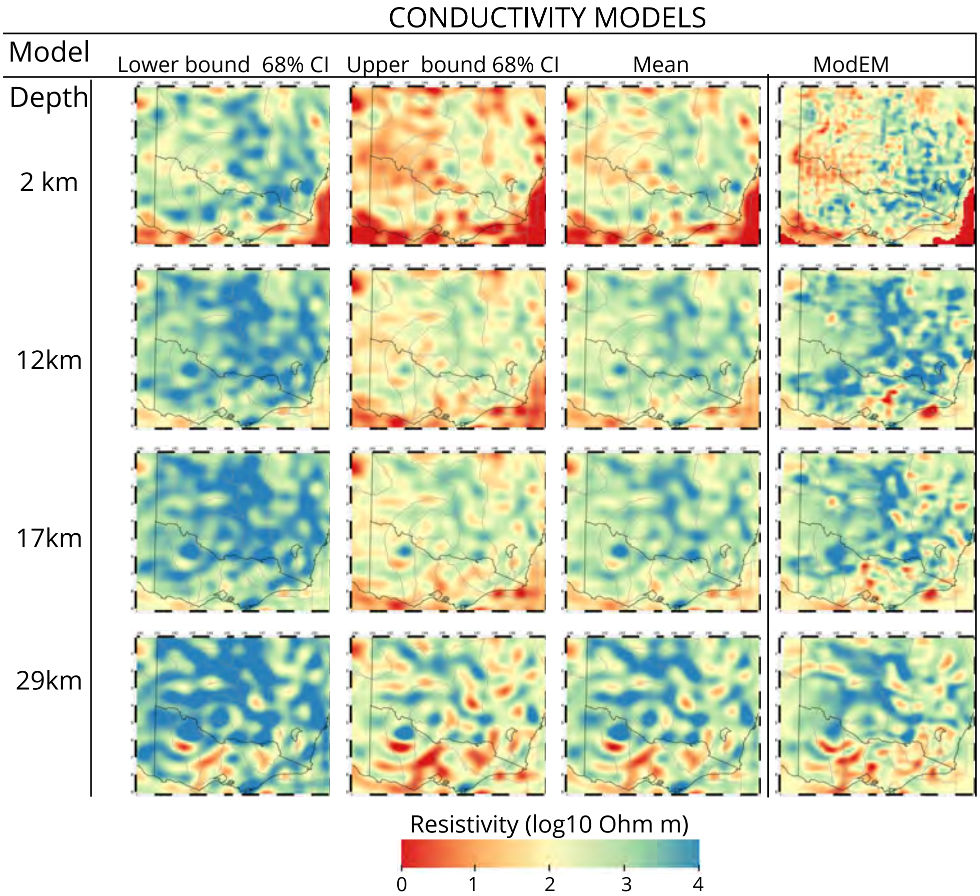

Figure 5. Conductivity in the crust from the joint probabilistic inversion. Columns (1)-(3): depth slices from the (1) the lower, (2) upper bound of the 68% percentile and (3) mean conductivity models of the posterior PDF. Column (4): conductivity model of (Kirkby et al., 2020). Selected depths are shown on the left of the figure and the boundaries of geological provinces are shown in grey lines.

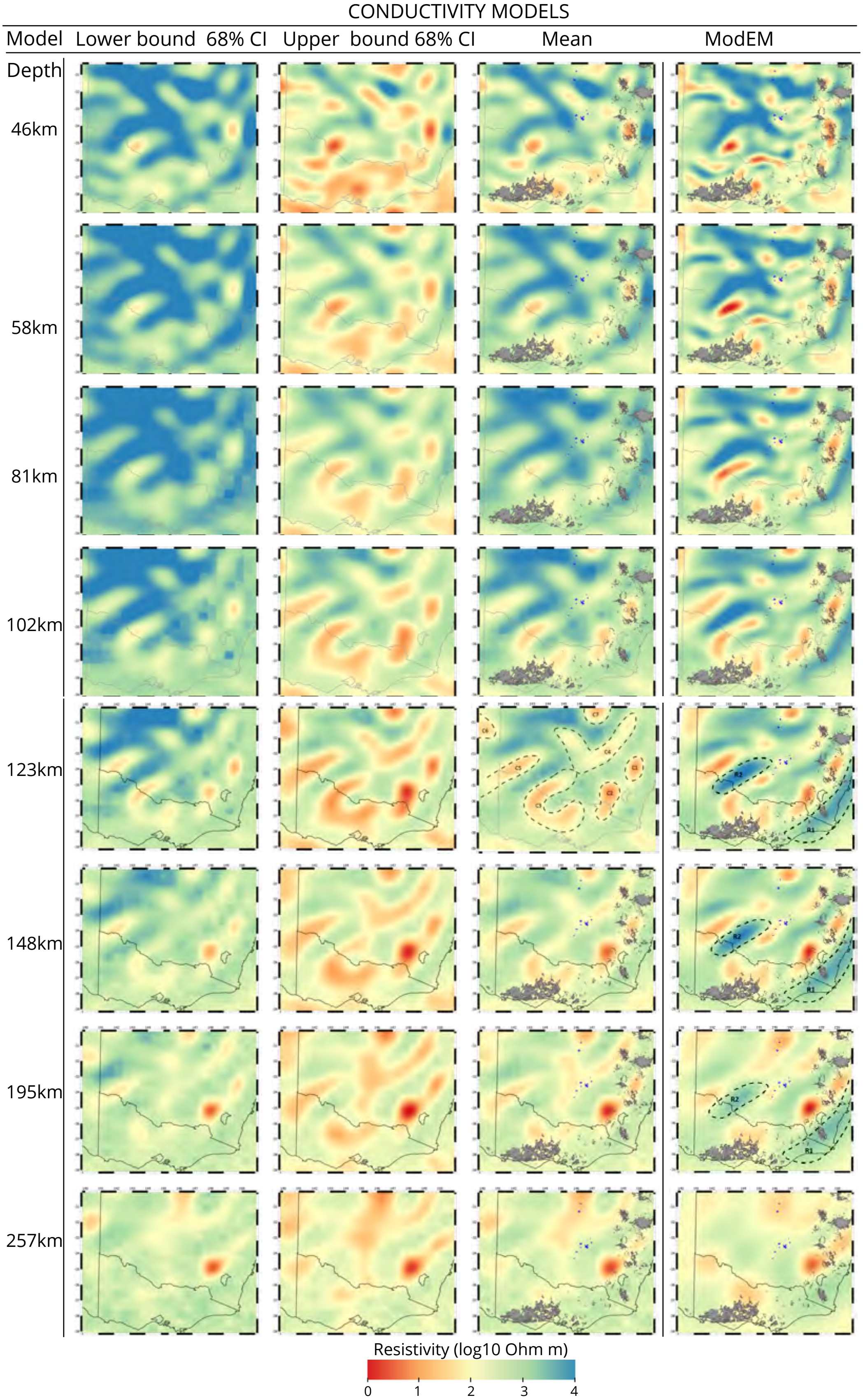

Figure 6. Mantle conductivity from the joint probabilistic inversion. Columns (1)-(3): depth slices from the (1) the lower, (2) upper bound of the 68% percentile and (3) mean conductivity models of the posterior PDF. Column (4): conductivity model of Kirkby et al. (2020). The location of leucitite- bearing volcanism are shown in blue and standard basaltic volcanoes in grey. Selected depths are shown on the left of the figure. Dashed-black lines highlight conductors in the mean model and resistors in the ModEM model below 123 km depth

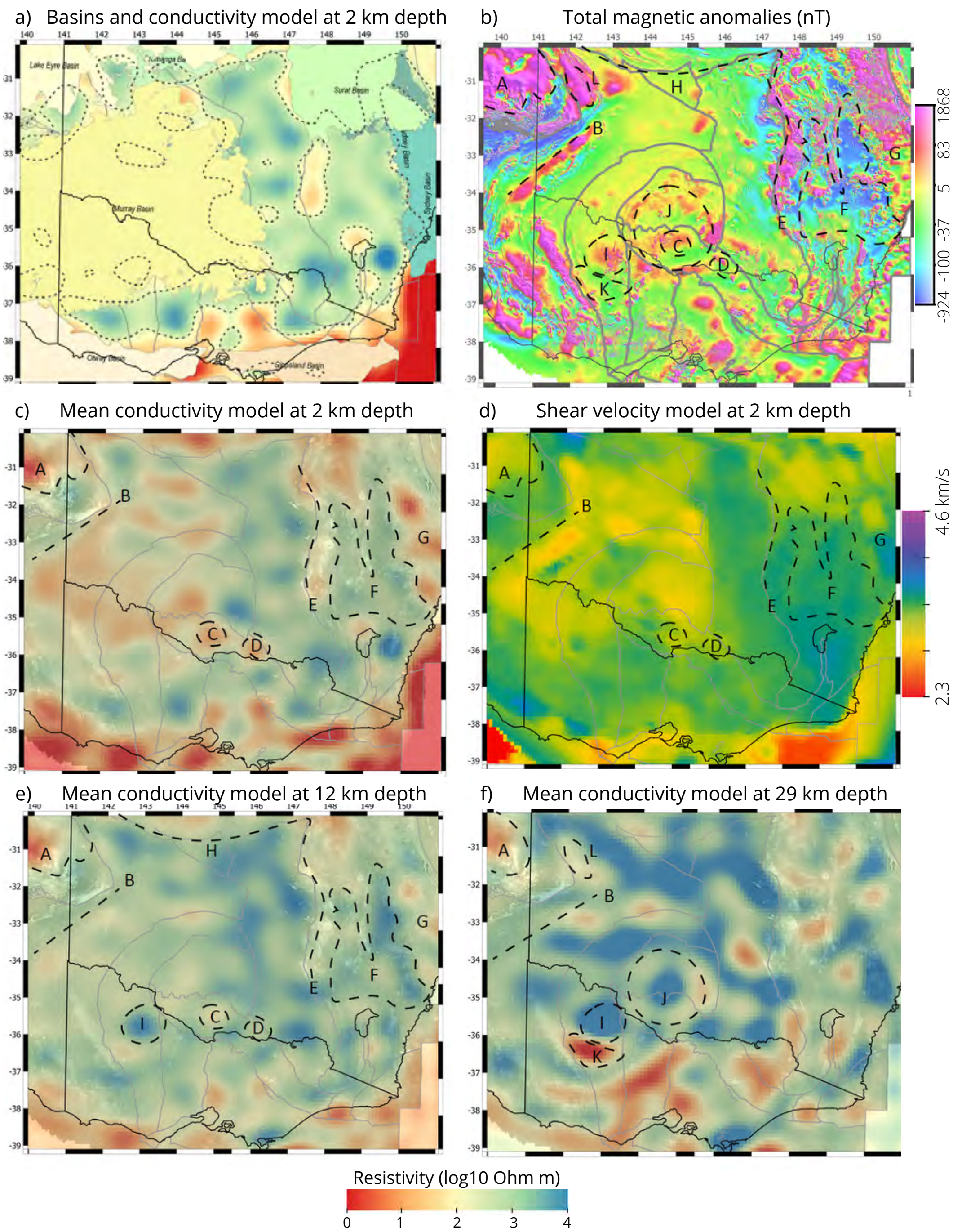

Figure 7. (a) Sedimentary basins overlying mean conductivity model at 2 km depth and 200 Ωm-resistivity contour in dash lines. (b) Total magnetic anomalies after Nakamura & Milligan (2015) (c) Mean conductivity (overlying the magnetic anomalies in grey scale) and (d) shear wave velocity model after Pilia et al. (2015) at 2 km depth. (e-f) Mean conductivity models at 12 and 29 km depth overlying the magnetic anomalies in grey scale. We refer the reader to the main text for a description of structures A-L. Boundaries of geological provinces are shown in grey lines.

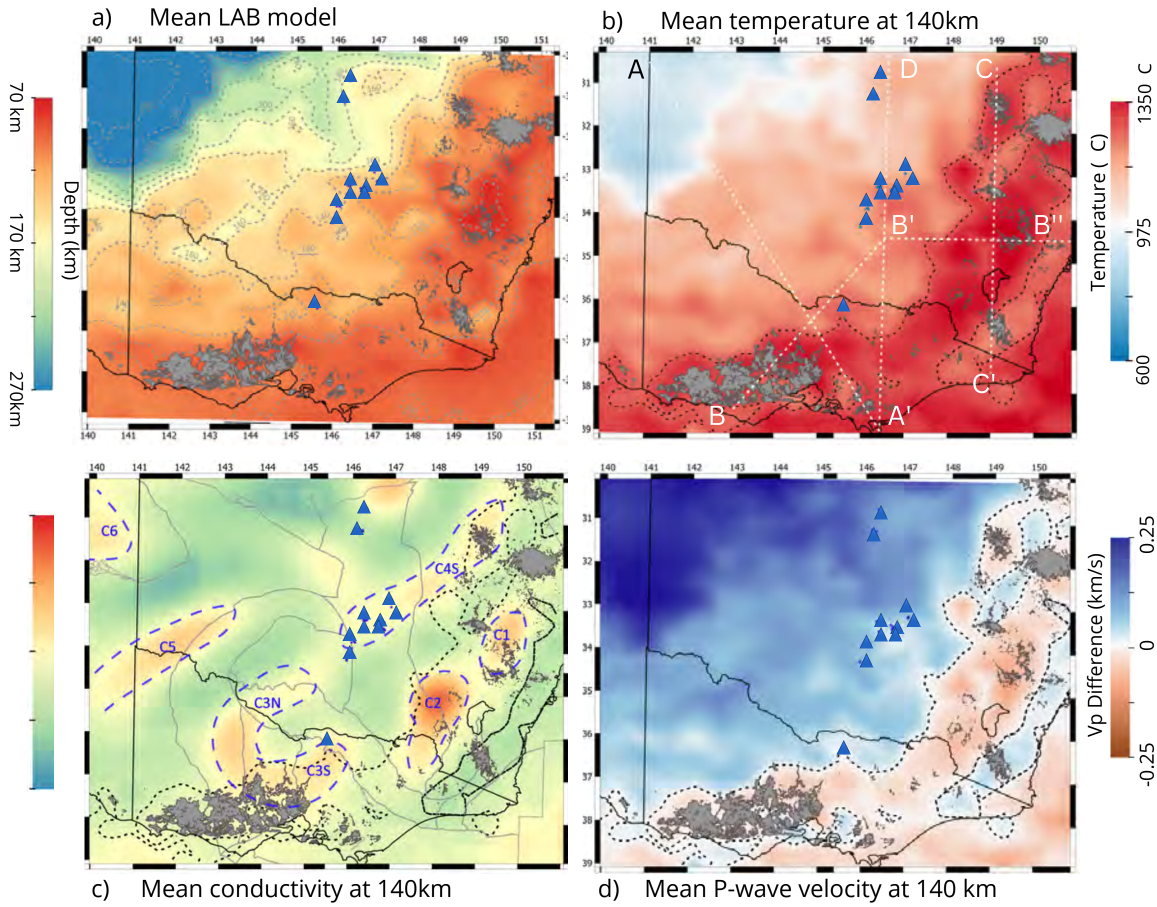

Figure 8. (a) Mean LAB depth. Contours of the LAB depth every 20 km are shown in grey-dashed line. Mean models at 140 km of (b) temperature (c) electrical conductivity and (d) P-wave velocity relative to 1-D reference model AusREM at $34.4^oS, 145^oE$. The 1250^oC-contour (corresponding with the thermal LAB) is plotted in dashed-black in (b-d). Panel (c) shows the location of the geological provinces and conductors in dashed blue. The location of leucitite volcanoes are shown in blue triangles and the surface outcrop of basaltic volcanics are shown in grey in all panels. Panel (b) shows five transects which are discussed in section 5.1.

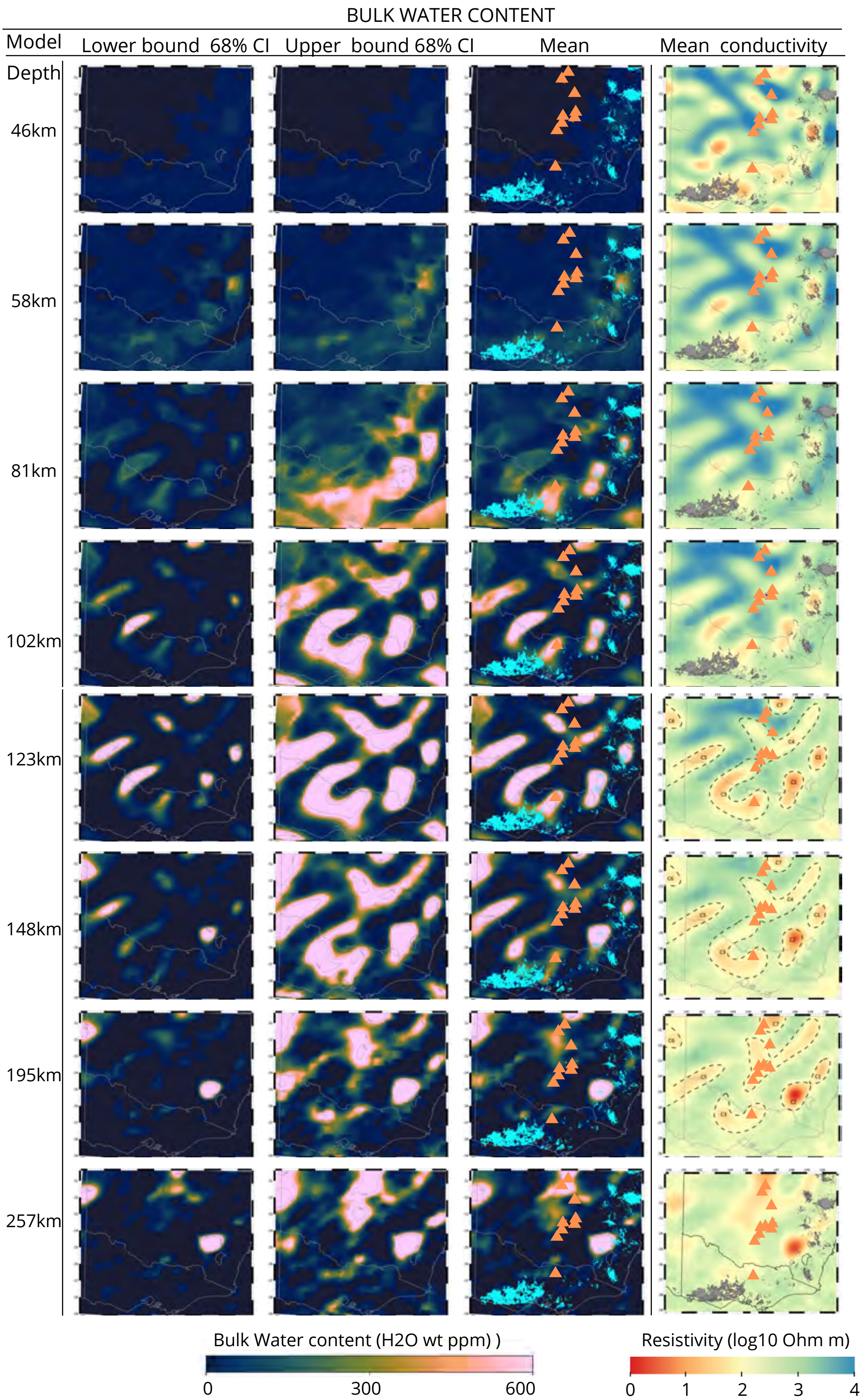

Figure 9. Bulk water content and mantle conductivity models from the joint probabilistic inversion. Columns (1)-(3): water content maps obtained from the (1) the lower, (2) upper bound of the 68% CI and (3) mean conductivity models. Column (4): depth slices from mean conductivity models of the posterior PDF. The location of leucitite- bearing volcanism and basaltic volcanoes are shown in orange and turquoise in (3); and blue and in grey in (4). Selected depths are shown on the left of the figure. We refer to the main text for an explanation of structures C1-C7. Selected depths are shown on the left of the figure.

the following structures (Figure 9): C_1, C_2 and C_3 beneath the eastern basaltic volcanoes; C_4 below the central leucitites; C_5 on the eastern boundary of Delamerian Orogen; C_6 beneath CP; and the deep localized conductor C_7 at $\sim -30.5^o N, 147^o E$, beneath the northern leucitites.

Figures 10-11.I and Figure S8 (Supplementary material) show vertical slices of the conductivity, water content and temperature along the four transects depicted in Panel (b) of Figure 8. The transects in Figure 10.I cross most of the geological provinces on the west and demonstrate a striking correlation between known geological boundaries and the alternation between wet/dry portions of the lithosphere. The joint assessment of these transects clearly shows that the lithospheric mantle beneath CP (C_6) corresponds to a highly conductive, hydrated, and cold region. We observe a high-conductivity anomaly (C_5) below the Stawell Zone that crosses the LAB. While the high temperatures found in this region (T_2 in Figure 10.Ic) can partially explain its conductivity structure, Figure 10.Ib indicates that a large part of this anomaly is related to metasomatism (or incipient melting?). The high-conductivities observed in region C_{3N} (beneath Tabberrabberra Zone) and the conductor C_{NV1} (at ∼90 km depth beneath the NV) can be entirely explained by a relatively large water content. We observe that while the conductivity of C_{3S} at $\sim$ 200 km can be explained by the high anomalous temperatures found in that region (T_1), a substantial part of its conductivity at $\sim$ 150 km is explained by the presence of water (or melt?). Two shallow conductors C_{NV2} and C_{NV3} are found at ∼20-75 km depth beneath the NV.

Along the transects in Figure 10.II, the LAB shows a small perturbation over a large conductive anomaly at $\sim$ 50 km and two defined steps at $\sim$ 300 and $\sim$ 750 km. These features correlate with the location of the northern leucitites, central leucitites and basaltic volcanoes, respectively. They also correlate with the location of high-conductivity regions (C_7, C_4 and C_{3S}) in the sub-lithosphere. Comparing the conductivity and bulk water content along this transect, we observe that while water contents at C_7 and C_4 are relatively large, that of C_{3S} is considerably lower. A series of crustal conductors are also observed beneath both the leucitites and basaltic volcanoes.

Figure 11.I, which transects across the eastern basaltic volcanoes and the NV, shows the continuation of C_{3S}, C_{NV2} and T_1 beneath the NV. A high-conductivity and wet region (C_1) is observed in the sub-lithospheric mantle below the Eastern Province. This deep, wet structure is also seen in Figure S8 and correlates with a high-temperature anomaly (T_3). A shallow semi-hydrated structure (C_{EP1}) is observed right below the basaltic volcanoes. The relationship between these features is hard to reconcile unless we relax the assumption that the entire conductivity anomaly over the background is due purely to water content. We discuss this further in the next section.

5 Discussion

5.1 Mantle metasomatism and volcanism in southeast Australia

Mantle metasomatism occurs when incipient melts or fluids react with mantle rocks (predominantly peridotite). These reactions can i) affect the modal proportions of peridotites, ii) introduce new volatile-bearing phases (phlogopite, amphibole, apatite, and carbonates) and, in some pervasive cases, iii) create new lithological domains, such as pyroxenite ± volatile-bearing phase lithologies (e.g. O'Reilly & Griffin, 1987). The generation of volatile-bearing phases reduces the solidus temperature (Wallace & Green, 1988; Foley et al., 2009; Pintér et al., 2021) and increases the electrical conductivity of the mantle domain (Selway, 2014).

The bulk water content we report in this study acts as a general proxy for metasomatism or mantle fertility, i.e., the inclusion of phases (metasomes) that increase the electrical conductivity of the mantle. Therefore, as mentioned above, this proxy lumps

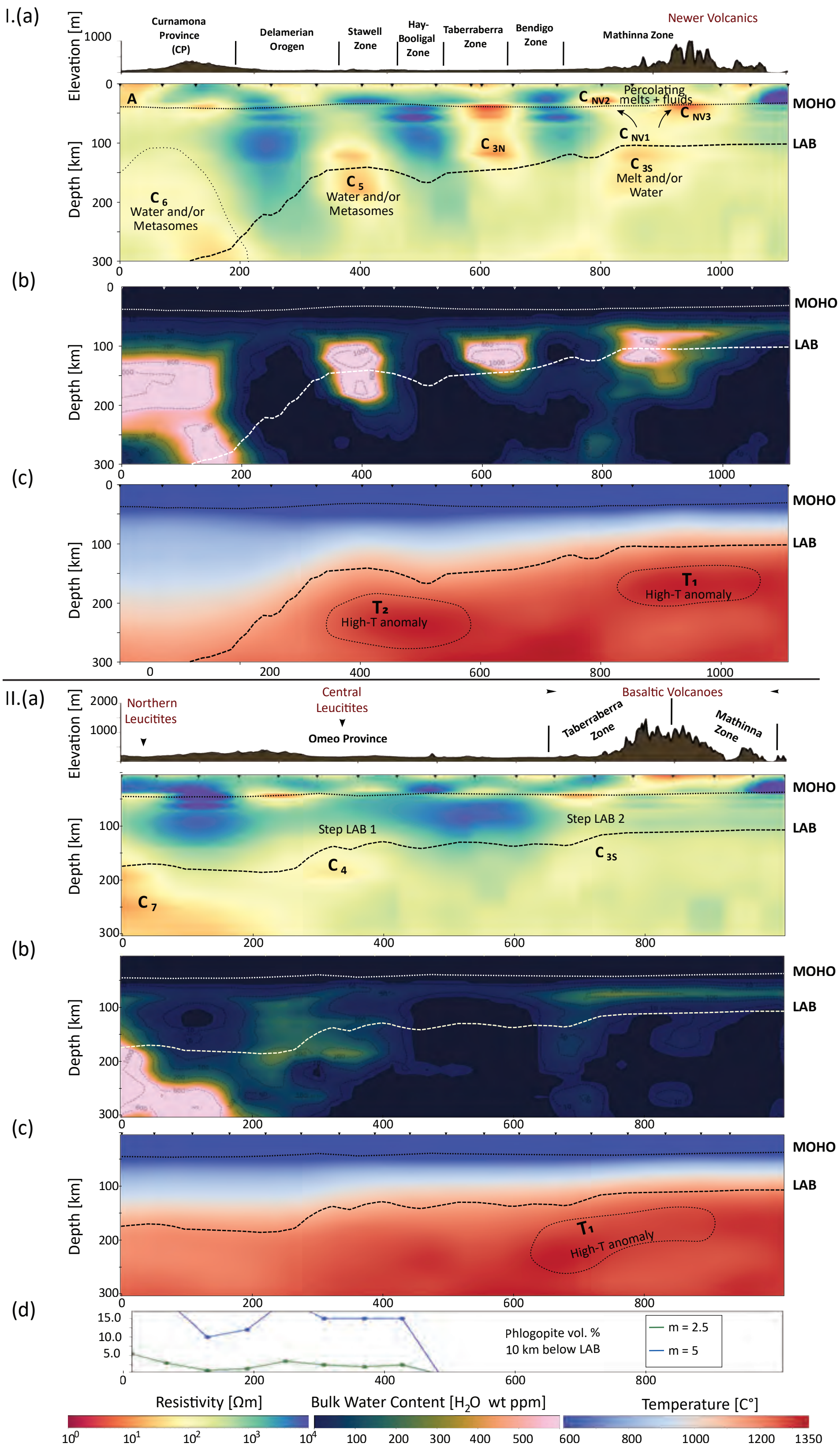

Figure 10. I.Vertical slices along transect A-A' (crossing most of the geological provinces) of a) the mean conductivity model, b) bulk water content derived from the mean conductivity mode and c) temperature. II. Vertical slices along transect D-A' (crossing the leucitite volcanics and basaltic volcanics in the south) of a) the mean conductivity model, b) bulk water content derived from the mean conductivity model and c) temperature. d) Intermediately connected (m=2.5 in blue) and poorly connected (m =5 in green) phlogopite in a dry lherzolitic matrix that fit the observed conductivities along the transect. The Moho and LAB depths along that transects are shown in dashed lines in all panels. The elevation and location of the geological provinces is shown at the top of the figures.

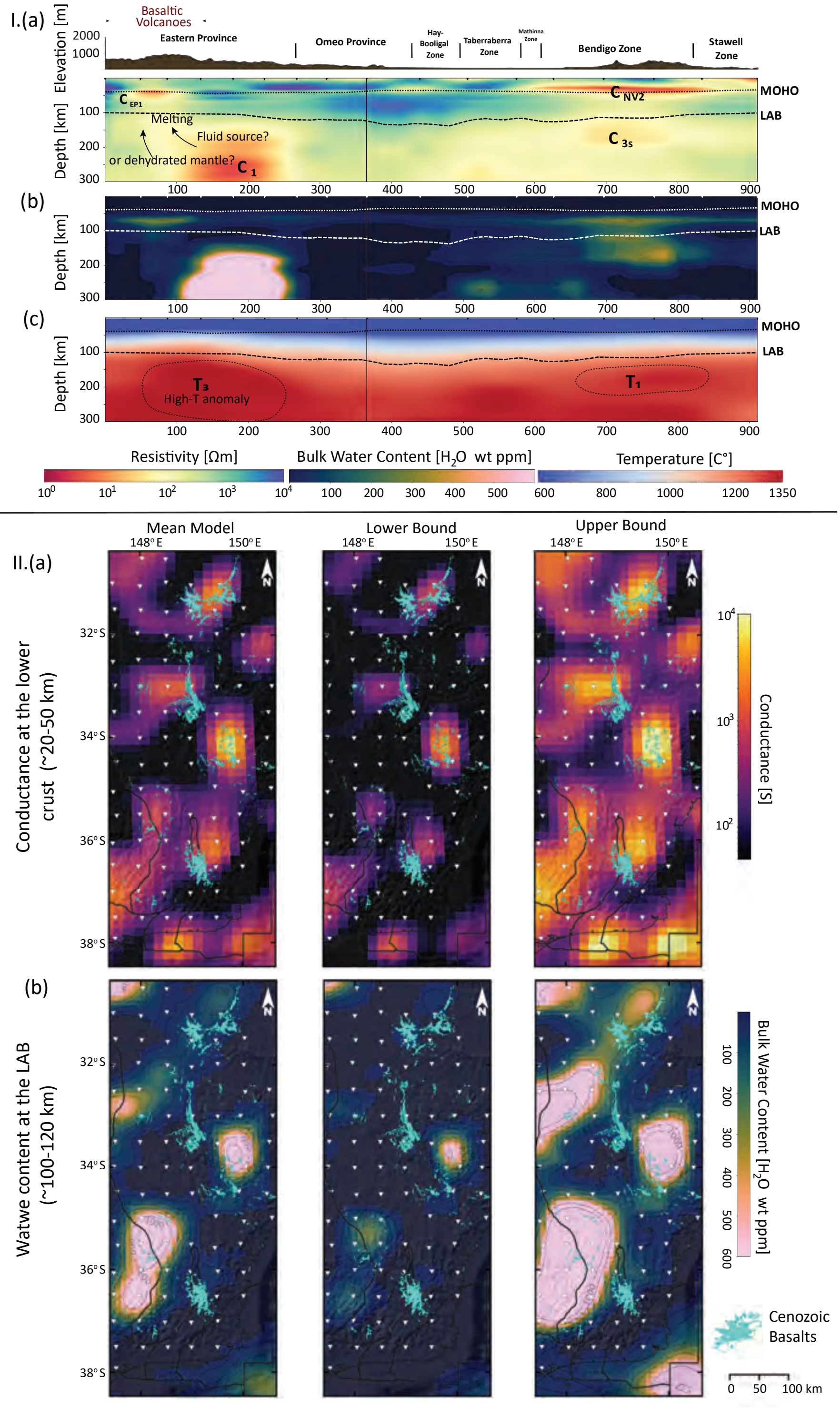

Figure 11. I.Vertical slices along transect B"-B'-B (across the basaltic eastern volcanoes and the NV) of a) the mean conductivity model, b) bulk water content derived from the mean conductivity model and c) temperature. The Moho and LAB depths along that transect are shown in dashed lines in all panels. The LAB depth along that transect is shown in dashed-black line in all panels. The elevation and location of the volcanics and the NV are shown at the top of the figure. II. Relationship between Cenozoic eastern volcanics and the parameters derived from the electrical conductivity model: (a) Conductance of the lower-crust ($\sim$ $20-50$ km), (b) water content calculated around the LAB depth ($\sim 100-120$ km).

together a number of factors not explicitly modeled in this work, for example, i) the presence of phases such as graphite or sulphides for depths above 75-120 km (Selway, 2014; Özaydın & Selway, 2020); ii) co-existing water and phlogopite in cold mantle below 75-120 km depth; or iii) presence of melt in regions of elevated temperatures.

The results of Section 4.4 indicate widespread mantle metasomatism in southeastern Australia (Figures 9-11.I). Clear correlations are observed between the location of volcanic centers and regions of metasomatized mantle and conductive crust. In particular, these regions are i) C_{3S}, C_{NV1}, C_{NV2} and C_{NV3} beneath Newer Volcanics; ii) C_1 and C_{EP1} beneath the Eastern Volcanics (also C_4, C_{EP2} and C_{EP3} Figure S8); iii) C_4 beneath Central Leucitites; and iv) C_7 below Northern Leucitites. Xenoliths entrained in these lavas show strong evidence for metasomatism in the source (Yaxley et al., 1991, 1998; Shea et al., 2022), further validating the presence of metasomatic agents in these regions (Frey et al., 1978). Other metasomatized mantle regions show a strong link with subduction/accretion processes rather than volcanism. These are C_6, C_5 and C_{3N} beneath CP, Stawell Zone and Taberraberra Zone, respectively.

One of the key benefit of our inversion is that we can dissociate the effects of the temperature from other factors controlling the conductivity structures and, ultimately, map anomalies associated with mantle metasomatism. While the current state of our methodology does not allow us to discriminate the different metasomatic factors (presence of melt, water or phlogopite, for example), these can be inferred via the joint assessment of the conductivity, temperature and metasomatism models in different regions. Further analysis with contributions from melt modeling may be required to understand the full-scope behind metasomatism and the genesis of melts in southeast Australia. This work is left for a forthcoming publication.

5.1.1 Basaltic volcanoes

The existence of shallow mantle upwellings and thin lithosphere provides a favorable setting for extensive decompression melting and mantle metasomatism (Aivazpourporgou et al., 2015). The LAB is very shallow in the Newer Volcanics (NV) and Eastern Volcanics (EV), allowing mantle upwellings to reach depths at which decompression melting of peridotitic rocks (and the resulting basaltic primitive melts) is possible. In this context, we also observe that the metasomatized regions C_{3S} and C_1 correlate with the location of sub-lithospheric high-temperature anomalies (T_1 and T_3, respectively). From the low-velocities observed at 60-80 km beneath the NV (Figure 4), Rawlinson et al. (2017) interpreted T_1 as a mantle upwelling and the source of the NV (see also Rawlinson et al., 2015). Similarly, Rawlinson et al. (2015) interpreted the low-velocity anomaly corresponding with T_3 (Figures 4) as a deep mantle source for the EV. All of the above point to ideal conditions for the generation of extensive basaltic magmatism in this region.

Figures 10.I and 11.I show a clear conductive pathway from C_{3S} to C_{NV1}-C_{NV3} and from C_1 to C_{EP1}, while the mantle beneath the volcanics is relatively dry. To further illustrate the relationship between the location of volcanics, shallow conductors and mantle metasomatism, Figure 11.II shows the average conductance at 20-50 km depth and average water content near the LAB beneath the EV. According to these results, basalt fields tend to associate with shallow conductors (Figure 11.IIa) and dry mantle (Figure 11.IIb). This relationship indicates that metasomatic agents percolated from deep mantle sources and traversed towards the crust. On their ascent, they precipitated conductive minerals forming shallow conductors (C_{NV2},C_{NV3}, C_{EP1}, C_{EP2}, C_{EP3} in Figures 10.I, 11.I and S8). We also note that basalts tend to be located in the surroundings of the most metasomatized regions of the lithosphere rather than on top of them; something that has been observed also in kimberlites worldwide (Özaydın & Selway, 2022).

The dry mantle beneath the basaltic fields suggests that the melting events exhausted the mantle source in the original metasomes and left behind drier residues.

5.1.2 Leucitite volcanoes

The leucitite lavas have melt compositions comparable to lamproites, and were derived from an atypical mantle assemblage of phlogopite-bearing pyroxenite (Shea et al., 2022; Foley et al., 2022). Due to these lava compositions, Kirkby et al. (2020) interpreted the conductors beneath the central leucitites as regions of metasomatised mantle with hydrous minerals such as phlogopite. Given the high conductivities ($< 100\Omega$ m) and bulk water content (~ 200 ppm) observed around C_4 (Figures 10.II), our results indicate a high probability for the presence of volatile-bearing minerals, supporting the above interpretation.

Using the water calculation setup described in Section 3.6 and the phlogopite conductivity model of Li et al. (2017), we calculated the electrical conductivities of lherzolite with 5 and 10 % vol. of 0.52 w.t. fluorine-bearing phlogopite (average fluorine value of mantle rocks, Özaydın et al., 2022) for both perfectly connected (m = 1.1, modified Archie's law) and sparsely populated phlogopites (m = 6, modified Archie's law). The results show that perfectly connected cases are 2.5 orders of magnitude more conductive than the observed conductivities in the region, while the conductivity for sparsely populated/disconnected cases lay near the lower bound of the observed conductivities (Figure S9 in Supplementary Material). These results suggest that a lherzolite with 5-10 % vol of partially connected ($6 < m < 1.1$) phlogopite explains the conductivities in C_4. We interpret the high conductivities in C_4 as a phlogopite-bearing lherzolite with small percentages of partially to sparsely connected phlogopite. These results are also illustrated in Figure 10.II.d , which shows the percentage of partially connected (m=2.5) phlogopite that can explain the observed conductivities beneath the leucitites volcanoes. We note that large amounts of phlogopite would drastically lower the seismic velocities (e.g., Selway et al., 2015), something not seen in our models. We therefore reject the hypothesis of large percentages ($\geq$ 15%) of poorly connected (m=5) phlogopites in this region.

The northern leucitites sit above a high-conductivity and metasomatized region below the LAB (C_7). The ultrapotassic compositions of these lavas suggest low-degree partial melting (Cundari, 1973), which is consistent with the relatively colder temperatures found in the region. Furthermore, potassium-rich magmas are produced by melting of a metasomatized mantle that has been enriched in phlogopite (Xu et al., 2017; Förster et al., 2019). We calculated the effect of phlogopites in this region and found similar results to those for the central leucitites (Figures S9), favoring the scenario with partially connected phlogopites. Compared to the central leucitites, the higher conductivities and colder temperature in this region provide favorable conditions for the presence of existing phlogopites that survived previous melting events.

5.1.3 Curnamona Province

Figure 10.I.a-b shows a successive alternation of conductive/wet and resistive/dry lithospheric domains that resemble the west-to-east subduction-accretion process in eastern Australia (Glen, 2005; Shea et al., 2022). The joint assessment of the fields depicted in Figure 10.I also suggests that the region C_6 experienced pervasive mantle metasomatism. Given the cold temperatures, the lack of present magmatism, and the geological history of southeastern Australia, the metasomatic events C_6 are likely related to accretion processes whereby successive subduction and orogenic events introduced metasomatic agents into the mantle. Overtime, this process preferentially metasomatized the old, thick lithosphere beneath Curnamona province.

The crustal conductors (A) below CP (described in Section 4.3.1) can be seen in Figure 10.Ia. Kay et al. (2022) interpreted these shallow conductors as the deposition of interconnected graphite. However, given that graphite films are not stable at shallow depths (Zhang & Yoshino, 2017; Yoshino et al., 2018), we observe that a more feasible explanation for these crustal conductors are carbon-rich fluids sourced from the deep metasomatized region C_6 (Thibault et al., 1992).

5.2 Implications for magma generation beneath eastern Australia

Age-progressive volcanism in the EAVP, particularly along the Cosgrove track (Davies et al., 2015), has been widely attributed to long-lived mantle plume activity (Wellman & McDougall, 1974). However, Shea et al. (2022) has recently argued that primitive melt compositions throughout the EAVP, including all or most of the age-progressive volcanism, were produced by melting of a metasomatized mantle source at temperatures lower than those expected in a deep mantle plume. The petrological and geochemical evidence summarized by Shea et al. (2022) and in the previous sections indicate that primitive melts, particularly those associated with the leucitites, originated from a pyroxenitic component rather than from a peridotitic mantle lithology. Since the solidi of pyroxenites (Foley et al., 2022) is substantially lower than that of anhydrous peridotites (Walter, 1998), partial melting of such lithologies is possible with only slight perturbations above ambient upper mantle temperatures. The lack of picrites within the EAVP, which are products of high-degrees of partial melting of peridotite, also suggest low-temperature, small degrees of partial melting dominated volcanism in the EAVP.

Our results show a series of steps in the LAB that correlate well with both the location of basaltic and leucitite volcanoes (Figures 10.II and 12). Thermomechanical models have shown that such steps in the LAB constitute areas prone to generating sublithospheric small-scale, edge-driven convection (EDC) instabilities and partial melting (e.g., Zlotnik et al., 2008; Van Wijk et al., 2010; Davies & Rawlinson, 2014; Ballmer et al., 2011; Afonso et al., 2008; Duvernay et al., 2021a). In particular, Duvernay et al. (2021b) showed that shear-driven upwelling (SDU) and EDC processes that account for water content in the upper mantle can produce enough melt to explain the total melt volume in the EAVP.

Considering all of the above, a plausible model arises for the melt generation in southeastern Australia, which we summarize in Figure 12. The relative motion of the Australian plate and the asthenospheric mantle created a favourable asthenospheric flow (possibly towards the south-southwest) which allowed the generation of EDC/SDU cells beneath steps in the LAB (e.g. above C_4 and C_{3S}). Such a convective flow can detach metasomatized lithologies from the lowermost portions of the lithosphere (on the thick side of the step) and drag them into the upwelling limbs of the EDC/SDU convection cell, where they would preferentially melt (given their lower solidus) and create the primary metasomatizing melts. The latter would subsequently react with the lower portions of the lithosphere (in the thin side of the LAB step) and create the source of the leucitite volcanoes. This scenario is similar to the one presented by Shea et al. (2022) and supported by our results and by the abundant petrological evidence summarized by these authors.

If EDC/SDU cells are the main driver for the leucitite volcanism, they need to be able to produce melts for a relatively short period of time (non regenerative) to explain the punctuated nature of this volcanism. Indeed, numerical simulations clearly show that ED/SD instabilities are ephemeral in nature and can be hindered by small perturbations in the sublithospheric flow (e.g., King & Anderson, 1995; Duvernay et al., 2021b, 2022). The presence of an anomalously hot upwelling or plume can also enhance or shut down melting near lithospheric steps (Mather et al., 2020; Duvernay et al., 2022), making it difficult to separate the two mechanisms without further knowledge on the underlying

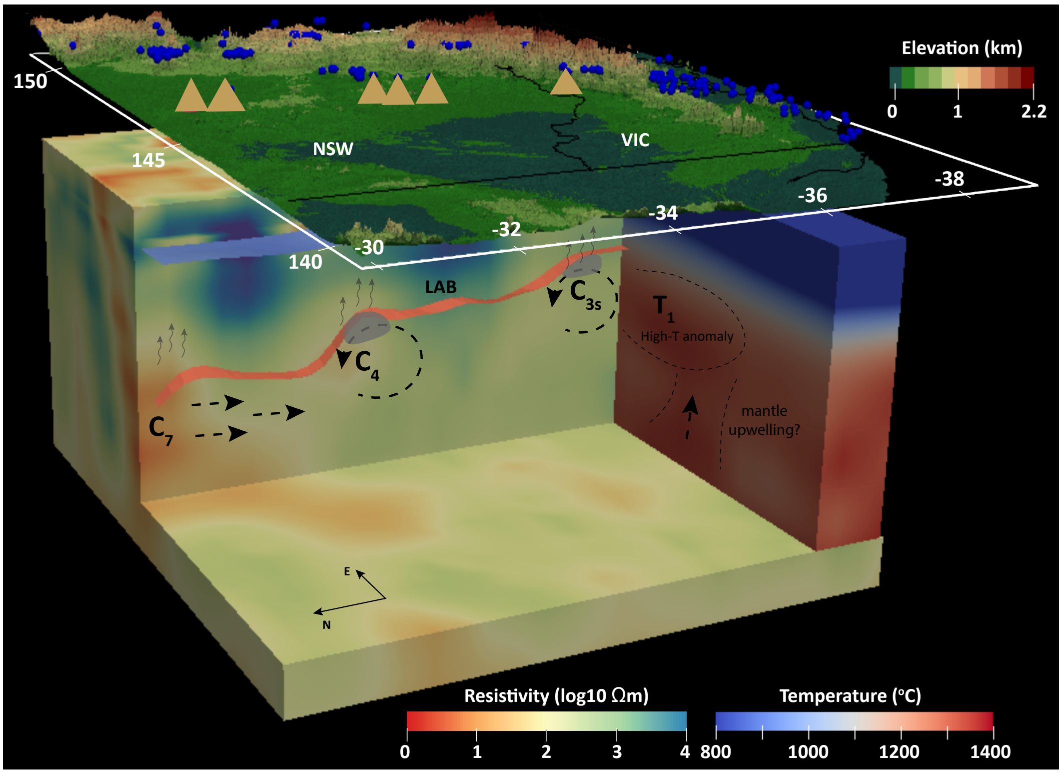

Figure 12. 3D rendering views of the LAB (red surface), mean conductivity and temperature models depicting interactions between mantle metasomatism and steps in the LAB. Dashed black arrows show the flow of the asthenosphere and shearing of enriched mantle material into EDC-cells (circular dashed lines). Local hotspots along the LAB where enriched mantle material crosses its solidus in the sub-lithospheric mantle are indicated by grey blobs. Grey arrows indicate incipient melts that may travel across the LAB from deep to shallow portions of the lithospheric mantle. Leucitites and basaltic volcanic centers are shown in yellow triangles and blue circles, respectively. The Moho is shown in blue over the conductivity model. The figure includes the topography in southeast Australia.

mantle dynamics. Thus, while our results provide a firm ground for interpretations on the origin of the EAVP and the roles that lithospheric structure and composition played, we cannot assess the deep mantle processes that controlled the large-scale sublithospheric flow.

6 Conclusions

We performed a joint probabilistic inversion of 3D magnetotellurics (MT) and seismic velocity data to constrain the lithospheric structure, metasomatic domains and melting processes in southeast Australia. Our methodology minimizes the non-uniqueness of the MT problem and provides quantitative information on model uncertainties via full posterior distributions. This information is crucial for assigning meaningful interpretations to electrical conductivity anomalies in terms of temperature versus metasomatism/compositional anomalies.

We image a highly heterogeneous lithosphere beneath eastern Australia that we link to geodynamic and tectono-magmatic processes across multiple scales. In particular, we detect widespread, but highly irregular mantle metasomatism throughout the region, pointing to complex interactions in the asthenosphere-lithosphere system. We also image alternating conductive/wet and resistive/dry lithospheric domains that correlate with the location of major geological provinces, resembling the west-to-east subduction-accretion process that formed eastern Australia. A series of steps in the present-day thermal structure correlate with the location of intra-plate volcanic centers and moderate thermal anomalies in the sublithospheric mantle, suggesting a genetic link between these three features. Basaltic volcanism is preferentially located in regions of very thin lithosphere and dry mantle, whereas leucitite volcanoes are located in regions of highly metasomatised mantle, intermediate lithospheric thickness and localized lithospheric steps. These results, together with recent petrological and geochemical evidence for relatively low temperatures in the melting region (Shea et al., 2022), suggest that the interaction between a complex, metasomatized lithospheric structure and localized mantle upwellings (e.g. via edge-driven convection or focusing of moderately hot mantle upwellings) are likely responsible for much of the volcanism in the EAVP, rather than a deep, hot mantle plume.

Lastly, it is generally accepted that metasomatized lithospheric mantle plays a critical role in the generation of major ore deposits. The ability to map metasomatized mantle domains paves the way to a new way of exploring for mineral resources.

Acknowledgments

The data is available at `https://www.github.com/manassero/Joint_Inv_SEAUS/tree/main/DATA`. We thank Nicholas Rawlinson and Simone Pilia for providing the seismic velocity models, and Anqi Zhang for providing interpolation subroutines. MCM thanks support from an International Macquarie Research Excellence Scholarship (iMQRES). MCM and JCA acknowledge support from ARC Grant DP160103502, ARC Linkage Grant LP170100233, the ARC Centre of Excellence Core to Crust Fluids Systems (http://www.ccfs.mq.edu.au) and Geoscience Australia. SÖ thanks the support from the Macquarie University COVID Recovery Fellowship fund and JJS was funded through ARC grant FL180100134. ST publishes with the permission of the Director of the Geological Survey of South Australia. AK and KC acknowledge the teams from GA, GSNSW, GSV, GSSA and the University of Adelaide involved in collecting the data and the support provided by individuals and communities to access the country, especially in remote and rural Australia. AK and KR publish with the permission of the CEO, Geoscience Australia. Resources from Macquarie University were used for this work.

References

Afonso, J. C., Fullea, J., Griffin, W., Yang, Y., Jones, A., Connolly, J., & O'Reilly, S. (2013a). 3-D multiobservable probabilistic inversion for the compositional and thermal structure of the lithosphere and upper mantle. I: A priori petrological information and geophysical observables. *Journal of Geophysical Research: Solid Earth*, *118*(5), 2586–2617.

Afonso, J. C., Fullea, J., Yang, Y., Connolly, J., & Jones, A. (2013b). 3-D multi-observable probabilistic inversion for the compositional and thermal structure of the lithosphere and upper mantle. II: General methodology and resolution analysis. *Journal of Geophysical Research: Solid Earth*, *118*(4), 1650–1676.

Afonso, J. C., Moorkamp, M., & Fullea, J. (2016). Imaging the lithosphere and upper mantle: Where we are at and where we are going. In N. L. M. Moorkamp P. Lelievre & A. Khan (Eds.), *Integrated imaging of the earth: Theory and applications* (pp. 191–218). John Wiley & Sons.

Afonso, J. C., Rawlinson, N., Yang, Y., Schutt, D. L., Jones, A. G., Fullea, J., & Griffin, W. L. (2016). 3-D multiobservable probabilistic inversion for the compositional and thermal structure of the lithosphere and upper mantle: III. Thermochemical tomography in the Western-Central US. *Journal of Geophysical Research: Solid Earth*, *121*(10), 7337–7370.

Afonso, J. C., Zlotnik, S., & Fernandez, M. (2008). Effects of compositional and rheological stratifications on small-scale convection under the oceans: Implications for the thickness of oceanic lithosphere and seafloor flattening. *Geophysical Research Letters*, *35*(20).

Aivazpourporgou, S., Thiel, S., Hayman, P. C., Moresi, L. N., & Heinson, G. (2015). Decompression melting driving intraplate volcanism in Australia: Evidence from magnetotelluric sounding. *Geophysical Research Letters*, *42*(2), 346–354.

Avdeeva, A., Moorkamp, M., Avdeev, D., Jegen, M., & Miensopust, M. (2015). Three-dimensional inversion of magnetotelluric impedance tensor data and full distortion matrix. *Geophysical Journal International*, *202*(1), 464–481.

Ballmer, M. D., Ito, G., Van Hunen, J., & Tackley, P. J. (2011). Spatial and temporal variability in Hawaiian hotspot volcanism induced by small-scale convection. *Nature Geoscience*, *4*(7), 457–460.

Bedrosian, P. A. (2016). Making it and breaking it in the Midwest: Continental assembly and rifting from modeling of EarthScope magnetotelluric data. *Precambrian Research*, *278*, 337–361.

Bell, D. R., Ihinger, P. D., & Rossman, G. R. (1995). Quantitative analysis of trace oh in garnet and pyroxenes. *American Mineralogist*, *80*(5-6), 465–474.

Bennington, N. L., Zhang, H., Thurber, C. H., & Bedrosian, P. A. (2015). Joint inversion of seismic and magnetotelluric data in the Parkfield Region of California using the normalized cross-gradient constraint. *Pure and Applied Geophysics*, *172*(5), 1033–1052.

Birch, W. D. (1978). Mineralogy and geochemistry of the leucitite at cosgrove, victoria. *Journal of the Geological Society of Australia*, *25*(7-8), 369–385.

Blackburn, G., Allison, G. B., & Leaney, F. W. J. (1982). Further evidence on the age of the tuff at mt gambier, south australia. *Transactions of the Royal Society of South Australia*, *106*, 163-167. Retrieved from https://archive.org/details/TransactionsRoy106Roya/mode/2up

Blatter, D., Key, K., Ray, A., Gustafson, C., & Evans, R. (2019). Bayesian joint inversion of controlled source electromagnetic and magnetotelluric data to image freshwater aquifer offshore New Jersey. *Geophysical Journal International*, *218*(3), 1822–1837.

Blatter, D., Naif, S., Key, K., & Ray, A. (2022). A plume origin for hydrous melt at the lithosphere–asthenosphere boundary. *Nature*, *604*(7906), 491–494.

Burdick, S., & Lekić, V. (2017). Velocity variations and uncertainty from transdimensional P-wave tomography of North America. *Geophysical Journal International*, *209*(2), 1337–1351.

Cayley, R. (2011). Exotic crustal block accretion to the eastern Gondwanaland margin in the Late Cambrian-Tasmania, the Selwyn Block, and implications for the Cambrian-Silurian evolution of the Ross, Delamerian, and Lachlan orogens. *Gondwana Research*, *19*(3), 628–649.

Cayley, R., & Musgrave, R. (2015). The Giant Lachlan Orocline—a powerful new predictive tool for mineral exploration under cover across eastern Australia. *Mines & Wines*, 29–38.

Champion, D. C., Brown, C., Mathews, E., Huston, D. L., & Kositcin, N. (2016). *Geodynamic synthesis of the Phanerozoic of eastern Australia.* Geoscience Australia.

Chave, A. D., & Jones, A. G. (2012). *The magnetotelluric method: Theory and practice.* Cambridge University Press.

Cline Ii, C., Faul, U., David, E., Berry, A., & Jackson, I. (2018). Redox-influenced seismic properties of upper-mantle olivine. *Nature*, *555*(7696), 355–358.

Cohen, B. E., Mark, D. F., Fallon, S. J., & Stephenson, P. J. (2017, 4). Holocene-neogene volcanism in northeastern australia: Chronology and eruption history. *Quaternary Geochronology*, *39*, 79-91. Retrieved from https://www.sciencedirect.com/science/article/pii/S1871101416300826 doi: 10.1016/J.QUAGEO.2017.01.003

Comeau, M. J., Unsworth, M. J., Ticona, F., & Sunagua, M. (2015). Magnetotelluric images of magma distribution beneath Volcán Uturuncu, Bolivia: Implications for magma dynamics. *Geology*, *43*(3), 243–246.

Connolly, J. (2009). The geodynamic equation of state: what and how. *Geochemistry, Geophysics, Geosystems*, *10*(10).

Cordell, D., Naif, S., Troch, J., & Huber, C. (2022). Constraining magma reservoir conditions by integrating thermodynamic petrological models and bulk resistivity from magnetotellurics. *Geochemistry, Geophysics, Geosystems*, *23*(9), e2022GC010455.

Cundari, A. (1973). Petrology of the leucite-bearing lavas in New South Wales. *Journal of the Geological Society of Australia*, *20*, 465-492. Retrieved from https://doi.org/10.1080/00167617308728829 doi: 10.1080/00167617308728829

Dai, L., & Karato, S.-i. (2009a). Electrical conductivity of orthopyroxene: Implications for the water content of the asthenosphere. *Proceedings of the Japan Academy, Series B*, *85*(10), 466–475.

Dai, L., & Karato, S.-i. (2009b). Electrical conductivity of pyrope-rich garnet at high temperature and high pressure. *Physics of the Earth and Planetary Interiors*, *176*(1-2), 83–88.

Davies, & Rawlinson, N. (2014). On the origin of recent intraplate volcanism in Australia. *Geology*, *42*(12), 1031–1034.

Davies, Rawlinson, N., Iaffaldano, G., & Campbell, I. H. (2015). Lithospheric controls on magma composition along Earth's longest continental hotspot track. *Nature*, *525*(7570), 511–514.

Demouchy, S., Shcheka, S., Denis, C. M., & Thoraval, C. (2017). Subsolidus hydrogen partitioning between nominally anhydrous minerals in garnet-bearing peridotite. *American Mineralogist: Journal of Earth and Planetary Materials*, *102*(9), 1822–1831.

Duvernay, T., Davies, D. R., Mathews, C., Gibson, A., & Kramer, S. (2021a). Linking intraplate volcanism to lithospheric structure and asthenospheric flow. *Geochemistry, Geophysics, Geosystems*, *22*, 1-29. doi: 10.1029/2021GC009953

Duvernay, T., Davies, D. R., Mathews, C. R., Gibson, A. H., & Kramer, S. C. (2021b). Linking intraplate volcanism to lithospheric structure and asthenospheric flow. *Geochemistry, Geophysics, Geosystems*, *22*(8), e2021GC009953.

Duvernay, T., Davies, D. R., Mathews, C. R., Gibson, A. H., & Kramer, S. C. (2022). Continental magmatism: The surface manifestation of dynamic interactions between cratonic lithosphere, mantle plumes and edge-driven convection. *Geochemistry, Geophysics, Geosystems*, *23*(7), e2022GC010363.

Evans, R. (2012). Conductivity of Earth materials. In J. A. Chave A. (Ed.), *The magnetotelluric method, theory and practice* (pp. 50–95). Cambridge: Cambridge Univ. Press New York.

Evans, R., Benoit, M. H., Long, M. D., Elsenbeck, J., Ford, H. A., Zhu, J., & Garcia, X. (2019). Thin lithosphere beneath the central Appalachian Mountains: A combined seismic and magnetotelluric study. *Earth and Planetary Science Letters*, *519*, 308–316.

Farquharson, C. G., & Oldenburg, D. W. (1998). Non-linear inversion using general measures of data misfit and model structure. *Geophysical Journal International*, *134*(1), 213–227.

Foley, S., Ezad, I., van der Laan Sieger, & Pertermann, M. (2022, 3). Melting of hydrous pyroxenites with alkali amphiboles in the continental mantle: 1. melting relations and major element compositions of melts. *Geoscience Frontiers*, 101380. Retrieved from https://linkinghub.elsevier.com/retrieve/pii/S1674987122000330 doi: 10.1016/j.gsf.2022.101380

Foley, S., Yaxley, G., Rosenthal, A., Buhre, S., Kiseeva, E., Rapp, R., & Jacob, D. (2009). The composition of near-solidus melts of peridotite in the presence of CO2 and H2O between 40 and 60ákbar. *Lithos*, *112*, 274–283.

Förster, M. W., Buhre, S., Xu, B., Prelević, D., Mertz-Kraus, R., & Foley, S. F. (2019). Two-stage origin of k-enrichment in ultrapotassic magmatism simulated by melting of experimentally metasomatized mantle. *Minerals*, *10*(1), 41.

Frey, F., Green, D., & Roy, S. (1978). Integrated models of basalt petrogenesis: a study of quartz tholeiites to olivine melilitites from south eastern Australia utilizing geochemical and experimental petrological data. *Journal of petrology*, *19*(3), 463–513.

Fullea, J., Muller, M., & Jones, A. (2011). Electrical conductivity of continental lithospheric mantle from integrated geophysical and petrological modeling: Application to the Kaapvaal Craton and Rehoboth Terrane, southern Africa. *Journal of Geophysical Research: Solid Earth*, *116*(B10), 94–105. doi: doi:10.1029/2011JB008544

Gallardo, L. A., & Meju, M. A. (2007). Joint two-dimensional cross-gradient imaging of magnetotelluric and seismic traveltime data for structural and lithological classification. *Geophysical Journal International*, *169*(3), 1261–1272.

García-Yeguas, A., Ledo, J., Piña-Varas, P., Prudencio, J., Queralt, P., Marcuello, A., … Pérez, N. (2017). A 3d joint interpretation of magnetotelluric and seismic tomographic models: The case of the volcanic island of Tenerife. *Computers & Geosciences*, *109*, 95–105.

Gardés, E., Gaillard, F., & Tarits, P. (2014). Toward a unified hydrous olivine electrical conductivity law. *Geochemistry, Geophysics, Geosystems*, *15*(12), 4984–5000.

Gilks, W. R., Richardson, S., & Spiegelhalter, D. (1995). *Markov chain Monte Carlo in practice*. Chapman and Hall/CRC.

Glen, R. (2005). The tasmanides of eastern australia. *Special Publication-Geological Society of London*, *246*, 23.

Glen, R. (2013). Refining accretionary orogen models for the Tasmanides of eastern Australia. *Australian Journal of Earth Sciences*, *60*(3), 315–370.

Glover, P. W. (2010). A generalized archie's law for n phases. *Geophysics*, *75*(6), E247–E265.

Goes, S., Govers, R., Vacher, & P. (2000). Shallow mantle temperatures under Europe from P and S wave tomography. *Journal of Geophysical Research: Solid Earth*, *105*(B5), 11153–11169.

Gregory, P. (2005). *Bayesian Logical Data Analysis for the Physical Sciences: A Comparative Approach with Mathematica® Support*. Cambridge University Press.

Griffin, W., Begg, G., & O'reilly, S. Y. (2013). Continental-root control on the genesis of magmatic ore deposits. *Nature Geoscience*, *6*(11), 905.

Griffin, W., Sutherland, F., & Hollis, J. (1987, 4). Geothermal profile and crust-mantle transition beneath east-central Queensland: Volcanology, xenolith petrology and seismic data. *Journal of Volcanology and Geothermal Research*, *31*, 177-203. Retrieved from https://www.sciencedirect.com/science/article/pii/0377027387900679 doi: 10.1016/0377-0273(87)90067-9

Haario, H., Laine, M., Mira, A., & Saksman, E. (2006). DRAM: efficient adaptive MCMC. *Statistics and computing*, *16*(4), 339–354.

Hassani, B., & Renaudin, A. (2013). The cascade bayesian approach for a controlled integration of internal data, external data and scenarios.

Haynes, M., Fomin, I., Afonso, J. C., Gorbatov, A., Czarnota, K., & Salajegheh, F.

(2020). *Developing thermochemical models of Australia's lithosphere.* Geoscience Australia.

Heinson, G., Didana, Y., Soeffky, P., Thiel, S., & Wise, T. (2018). The crustal geophysical signature of a world-class magmatic mineral system. *Scientific reports*, *8*(1), 1–6.

Heinson, G., Duan, J., Kirkby, A., Robertson, K., Thiel, S., Aivazpourporgou, S., & Soyer, W. (2021). Lower crustal resistivity signature of an orogenic gold system. *Scientific Reports*, *11*(1), 1–7.

Irving, A. J. (1980). Petrology and geochemistry of composite ultramafic xenoliths in alkalic basalts and implications for magmatic processes within the mantle. *American Journal of Science*, *280*, 389-416.

Jegen, M. D., Hobbs, R. W., Tarits, P., & Chave, A. (2009). Joint inversion of marine magnetotelluric and gravity data incorporating seismic constraints: Preliminary results of sub-basalt imaging off the Faroe Shelf. *Earth and Planetary Science Letters*, *282*(1-4), 47–55.

Johnson, R. W., Johnson, R. W., Knutson, J., & Taylor, S. R. (1989). *Intraplate volcanism: in eastern Australia and New Zealand.* Cambridge University Press.

Jones, A. G. (1999). Imaging the continental upper mantle using electromagnetic methods. *Lithos*, *48*(1-4), 57–80.

Jones, A. G. (2011). Three-dimensional galvanic distortion of three-dimensional regional conductivity structures: Comment on" three-dimensional joint inversion for magnetotelluric resistivity and static shift distributions in complex media" by Yutaka Sasaki and Max A. Meju. *Journal of Geophysical Research. Solid Earth*, *116*(12).

Jones, A. G., Afonso, J. C., & Fullea, J. (2017). Geochemical and geophysical constrains on the dynamic topography of the Southern African Plateau. *Geochemistry, Geophysics, Geosystems*, *18*(10), 3556–3575.

Karato, S.-i. (1990). The role of hydrogen in the electrical conductivity of the upper mantle. *Nature*, *347*(6290), 272.

Karato, S.-i. (2006). Remote sensing of hydrogen in earth's mantle. *Reviews in Mineralogy and Geochemistry*, *62*(1), 343–375.

Kay, B., Heinson, G., & Brand, K. (2022). Crustal magnetotelluric imaging of a Paleoproterozoic graphitic suture zone, Curnamona Province, Australia. *Gondwana Research*, *106*, 1–14.

Kelbert, A., Meqbel, N., Egbert, G. D., & Tandon, K. (2014). ModEM: A modular system for inversion of electromagnetic geophysical data. *Computers & Geosciences*, *66*, 40–53.

Kennett, B., & Salmon, M. (2012). Ausrem: Australian seismological reference model. *Australian Journal of Earth Sciences*, *59*(8), 1091–1103.

Khan, A. (2016). On Earth's mantle constitution and structure from joint analysis of geophysical and laboratory-based data: An example. *Surveys in Geophysics*, *37*(1), 149–189.

Khan, A., Connolly, J., & Olsen, N. (2006). Constraining the composition and thermal state of the mantle beneath europe from inversion of long-period electromagnetic sounding data. *Journal of Geophysical Research: Solid Earth*, *111*(B10).

King, S. D., & Anderson, D. L. (1995). An alternative mechanism of flood basalt formation. *Earth and Planetary Science Letters*, *136*(3-4), 269–279.

Kirkby, A., Czarnota, K., Huston, D. L., Champion, D. C., Doublier, M. P., Bedrosian, P. A., . . . Heinson, G. (2022). Lithospheric conductors reveal source regions of convergent margin mineral systems. *Scientific Reports*, *12*(1), 1–10.

Kirkby, A., Musgrave, R. J., Czarnota, K., Doublier, M. P., Duan, J., Cayley, R. A., & Kyi, D. (2020). Lithospheric architecture of a Phanerozoic orogen from magnetotellurics: AusLAMP in the Tasmanides, southeast Australia. *Tectonophysics*, *793*, 228560.

Li, Y., Jiang, H., & Yang, X. (2017). Fluorine follows water: Effect on electrical conductivity of silicate minerals by experimental constraints from phlogopite. *Geochimica et Cosmochimica Acta*, *217*, 16–27.

Liao, C., Hu, X., Zhang, S., Li, X., Yin, Q., Zhang, Z., & Zhang, L. (2022). Joint inversion of gravity, magnetotelluric and seismic data using the alternating direction method of multipliers. *Geophysical Journal International*, *229*(1), 203–218.

Liu, H., Zhu, Q., & Yang, X. (2019). Electrical conductivity of oh-bearing omphacite and garnet in eclogite: the quantitative dependence on water content. *Contributions to Mineralogy and Petrology*, *174*(7), 1–15.

Lu, J., Griffin, W. L., Tilhac, R., Xiong, Q., Zheng, J., & O'Reilly, S. Y. (2018). Tracking deep lithospheric events with garnet-websterite xenoliths from southeastern Australia. *Journal of Petrology*, *59*(5), 901–930.

Manassero, M. C., Afonso, J. C., Zyserman, F., Jones, A., Zlotnik, S., & Fomin, I. (2021). A Reduced Order Approach for Probabilistic Inversions of 3D Magnetotelluric Data II: Joint Inversion of MT and Surface-Wave Data. *Journal of Geophysical Research: Solid Earth*, *126*(12), e2021JB021962.

Manassero, M. C., Afonso, J. C., Zyserman, F., Zlotnik, S., & Fomin, I. (2020). A Reduced Order Approach for Probabilistic Inversions of 3D Magnetotelluric Data I: General Formulation. *Geophysical Journal International*, *223*(3), 1837–1863.

Mather, B. R., Müller, R. D., Seton, M., Ruttor, S., Nebel, O., & Mortimer, N. (2020). Intraplate volcanism triggered by bursts in slab flux. *Science advances*, *6*(51), eabd0953.

Miensopust, M. P., Queralt, P., Jones, A. G., & modellers, D. M. (2013). Magnetotelluric 3-D inversion—a review of two successful workshops on forward and inversion code testing and comparison. *Geophysical Journal International*, *193*(3), 1216–1238.

Moorkamp, M., Jones, A., & Eaton, D. (2007). Joint inversion of teleseismic receiver functions and magnetotelluric data using a genetic algorithm: Are seismic velocities and electrical conductivities compatible? *Geophysical Research Letters*, *34*(16).

Moorkamp, M., Jones, A., & Fishwick, S. (2010). Joint inversion of receiver functions, surface wave dispersion, and magnetotelluric data. *Journal of Geophysical Research: Solid Earth*, *115*(B4).

Moresi, L., Betts, P. G., Miller, M. S., & Cayley, R. A. (2014). Dynamics of continental accretion. *Nature*, *508*(7495), 245–248.

Musgrave, R. (2015). Oroclines in the Tasmanides. *Journal of Structural Geology*, *80*, 72–98.

Musgrave, R., & Rawlinson, N. (2010). Linking the upper crust to the upper mantle: comparison of teleseismic tomography with long-wavelength features of the gravity and magnetic fields of southeastern Australia. *Exploration Geophysics*, *41*(2), 155–162.

Naif, S., Selway, K., Murphy, B. S., Egbert, G., & Pommier, A. (2021). Electrical conductivity of the lithosphere-asthenosphere system. *Physics of the Earth and Planetary Interiors*, *313*(2021), 10661.

Nakamura, A. (2016). *Isostatic residual gravity anomaly grid of onshore Australia 2016.*

Nakamura, A., & Milligan, P. (2015). *Total magnetic intensity (TMI) colour composite image. Canberra: Geoscience Australia.*

Novella, D., Frost, D. J., Hauri, E. H., Bureau, H., Raepsaet, C., & Roberge, M. (2014). The distribution of h2o between silicate melt and nominally anhydrous peridotite and the onset of hydrous melting in the deep upper mantle. *Earth and Planetary Science Letters*, *400*, 1–13.

O'Reilly, S., & Griffin, W. (1987). Eastern Australia-4000 kilometres of mantle samples. In *Mantle zenoliths* (pp. 267–280). John Wiley & Sons.

Özaydın, S., & Selway, K. (2020). MATE: An analysis tool for the interpretation of magnetotelluric models of the mantle. *Geochemistry, Geophysics, Geosystems*, *21*(9), e2020GC009126.

Özaydın, S., & Selway, K. (2022). The relationship between kimberlitic magmatism and electrical conductivity anomalies in the mantle. *Geophysical Research Letters*, e2022GL099661.

Özaydın, S., Selway, K., Griffin, W. L., & Moorkamp, M. (2022). Probing the southern African lithosphere with magnetotellurics: 2. Linking electrical conductivity, composition, and tectonomagmatic evolution. *Journal of Geophysical Research: Solid Earth*, *127*(3), e2021JB023105.

Padrón-Navarta, J. A., & Hermann, J. (2017). A subsolidus olivine water solubility equation for the earth's upper mantle. *Journal of Geophysical Research: Solid Earth*, *122*(12), 9862–9880.

Pilia, S., Rawlinson, N., Cayley, R., Bodin, T., Musgrave, R., Reading, A., ... Young, M. (2015). Evidence of micro-continent entrainment during crustal accretion. *Scientific reports*, *5*(1), 1–6.

Pintér, Z., Foley, S. F., Yaxley, G. M., Rosenthal, A., Rapp, R. P., Lanati, A. W., & Rushmer, T. (2021). Experimental investigation of the composition of incipient melts in upper mantle peridotites in the presence of CO2 and H2O. *Lithos*, *396*, 106224.

Rawlinson, N., Davies, D., & Pilia, S. (2017). The mechanisms underpinning Cenozoic intraplate volcanism in eastern Australia: Insights from seismic tomography and geodynamic modeling. *Geophysical Research Letters*, *44*(19), 9681–9690.

Rawlinson, N., Kennett, B., Salmon, M., & Glen, R. (2015). Origin of lateral heterogeneities in the upper mantle beneath south-east Australia from seismic tomography. In *The earth's heterogeneous mantle* (pp. 47–78). Springer.

Rawlinson, N., Pilia, S., Young, M., Salmon, M., & Yang, Y. (2016). Crust and upper mantle structure beneath southeast Australia from ambient noise and teleseismic tomography. *Tectonophysics*, *689*, 143–156.

Raymond, O., Liu, S., Gallagher, R., Zhang, W., & Highet, L. (2012). Surface geology of Australia 1: 1 million scale dataset 2012 edition. *Geoscience Australia, Canberra*.

Raymond, O., Totterdell, J., Stewart, A., & Woods, M. (2018). Australian Geological Provinces, 2018. *Geoscience Australia, Canberra*.

Robertson, K., Heinson, G., & Thiel, S. (2016). Lithospheric reworking at the Proterozoic–Phanerozoic transition of Australia imaged using AusLAMP Magnetotelluric data. *Earth and Planetary Science Letters*, *452*, 27–35.

Rosas-Carbajal, M., Linde, N., Kalscheuer, T., & Vrugt, J. A. (2013). Two-dimensional probabilistic inversion of plane-wave electromagnetic data: methodology, model constraints and joint inversion with electrical resistivity data. *Geophysical Journal International*, *196*(3), 1508–1524.

Rosenbaum, G. (2018). The Tasmanides: Phanerozoic tectonic evolution of eastern Australia. *Annual Review of Earth and Planetary Sciences*, *46*, 291–325.

Selway, K. (2014). On the causes of electrical conductivity anomalies in tectonically stable lithosphere. *Surveys in Geophysics*, *35*(1), 219–257.

Selway, K., Ford, H., & Kelemen, P. (2015). The seismic mid-lithosphere discontinuity. *Earth and Planetary Science Letters*, *414*, 45–57.

Selway, K., & O'Donnell, J. (2019). A small, unextractable melt fraction as the cause for the low velocity zone. *Earth and Planetary Science Letters*, *517*, 117–124.

Shea, J. J., Ezad, I. S., Foley, S. F., & Lanati, A. W. (2022, 8). The eastern australian volcanic province, its primitive melts, constraints on melt sources and the influence of mantle metasomatism. *Earth-Science Reviews*, 104168. Retrieved from `https://linkinghub.elsevier.com/retrieve/pii/S0012825222002525` doi:

10.1016/j.earscirev.2022.104168
Smith, B. W., & Prescott, J. R. (1987). Thermoluminescence dating of the eruption at mt schank, south australia. *Australian Journal of Earth Sciences*, *34*, 335-342. doi: 10.1080/08120098708729415
Snyder, D., Hillier, M., Kjarsgaard, B., De Kemp, E., & Craven, J. (2014). Lithospheric architecture of the Slave craton, northwest Canada, as determined from an interdisciplinary 3-D model. *Geochemistry, Geophysics, Geosystems*, *15*(5), 1895–1910.
Stixrude, L., & Lithgow-Bertelloni, C. (2011). Thermodynamics of mantle minerals-ii. phase equilibria. *Geophysical Journal International*, *184*(3), 1180–1213.
Sutherland, F., Graham, I., Meffre, S., Zwingmann, H., & Pogson, R. (2012). Passive-margin prolonged volcanism, East Australian Plate: outbursts, progressions, plate controls and suggested causes. *Australian Journal of Earth Sciences*, *59*(7), 983–1005.
Takam Takougang, E. M., Harris, B., Kepic, A., & Le, C. V. (2015). Cooperative joint inversion of 3D seismic and magnetotelluric data: With application in a mineral province. *Geophysics*, *80*(4), R175–R187.
Tarantola, A. (2005). *Inverse problem theory and methods for model parameter estimation* (Vol. 89). siam.
Tesauro, M., Kaban, M. K., & Aitken, A. R. (2020). Thermal and compositional anomalies of the Australian upper mantle from seismic and gravity data. *Geochemistry, Geophysics, Geosystems*, *21*(11), e2020GC009305.
Thibault, Y., Edgar, A. D., & Lloyd, F. E. (1992). Experimental investigation of melts from a carbonated phlogopite lherzolite: implications for metasomatism in the continental lithospheric mantle. *American Mineralogist*, *77*(7-8), 784–794.
Thiel, S., & Heinson, G. (2013). Electrical conductors in Archean mantle—result of plume interaction? *Geophysical Research Letters*, *40*(12), 2947–2952.
Trampert, J., Vacher, P., & Vlaar, N. (2001). Sensitivities of seismic velocities to temperature, pressure and composition in the lower mantle. *Physics of the Earth and Planetary Interiors*, *124*(3-4), 255–267.
Van Wijk, J., Baldridge, W., Van Hunen, J., Goes, S., Aster, R., Coblentz, D., … Ni, J. (2010). Small-scale convection at the edge of the Colorado Plateau: Implications for topography, magmatism, and evolution of Proterozoic lithosphere. *Geology*, *38*(7), 611–614.
Wallace, M. E., & Green, D. H. (1988). An experimental determination of primary carbonatite magma composition. *Nature*, *335*(6188), 343–346.
Walter, M. J. (1998). Melting of garnet peridotite and the origin of komatiite and depleted lithosphere. *Journal of petrology*, *39*(1), 29–60.
Wannamaker, P. E., Evans, R. L., Bedrosian, P. A., Unsworth, M. J., Maris, V., & McGary, R. S. (2014). Segmentation of plate coupling, fate of subduction fluids, and modes of arc magmatism in Cascadia, inferred from magnetotelluric resistivity. *Geochemistry, Geophysics, Geosystems*, *15*(11), 4230–4253.
Wannamaker, P. E., Hasterok, D. P., Johnston, J. M., Stodt, J. A., Hall, D. B., Sodergren, T. L., … others (2008). Lithospheric dismemberment and magmatic processes of the Great Basin–Colorado Plateau transition,Utah, implied from magnetotellurics. *Geochemistry, Geophysics, Geosystems*, *9*(5).
Wei, W., Unsworth, M., Jones, A., Booker, J., Tan, H., Nelson, D., … others (2001). Detection of widespread fluids in the Tibetan crust by magnetotelluric studies. *Science*, *292*(5517), 716–719.
Wellman, P., & McDougall, I. (1974). Cainozoic igneous activity in eastern Australia. *Tectonophysics*, *23*(1-2), 49–65.
Withers, A. C., Bureau, H., Raepsaet, C., & Hirschmann, M. M. (2012). Calibration of infrared spectroscopy by elastic recoil detection analysis of h in synthetic olivine. *Chemical Geology*, *334*, 92–98.

Wu, P., Tan, H., Ding, Z., Kong, W., Peng, M., Wang, X., & Xu, L. (2022). Joint inversion of 3-D magnetotelluric and ambient noise dispersion data sets with cross-gradient constraints: methodology and application. *Geophysical Journal International*, *230*(1), 714–732.

Xu, B., Griffin, W. L., Xiong, Q., Hou, Z.-Q., O'Reilly, S. Y., Guo, Z., … Zheng, Y.-C. (2017). Ultrapotassic rocks and xenoliths from South Tibet: Contrasting styles of interaction between lithospheric mantle and asthenosphere during continental collision. *Geology*, *45*(1), 51–54.

Yaxley, G., Crawford, A., & Green, D. (1991, 11). Evidence for carbonatite metasomatism in spinel peridotite xenoliths from western Victoria, Australia. *Earth and Planetary Science Letters*, *107*, 305-317. Retrieved from `https://linkinghub.elsevier.com/retrieve/pii/0012821X9190078V` doi: 10.1016/0012-821X(91)90078-V

Yaxley, G., Green, D., & Kamenetsky, V. (1998, 11). Carbonatite metasomatism in the Southeastern Australian lithosphere. *Journal of Petrology*, *39*, 1917-1930. Retrieved from `http://dx.doi.org/10.1093/petroj/39.11-12.1917` (10.1093/petroj/39.11-12.1917)

Yoshino, T. (2010). Laboratory electrical conductivity measurement of mantle minerals. *Surveys in Geophysics*, *31*(2), 163–206.

Yoshino, T., Gruber, B., & Reinier, C. (2018). Effects of pressure and water on electrical conductivity of carbonate melt with implications for conductivity anomaly in continental mantle lithosphere. *Physics of the Earth and Planetary Interiors*, *281*, 8–16.

Young, M., Cayley, R., McLean, M., Rawlinson, N., Arroucau, P., & Salmon, M. (2013). Crustal structure of the east gondwana margin in southeast australia revealed by transdimensional ambient seismic noise tomography. *Geophysical Research Letters*, *40*(16), 4266–4271.

Yu, Y., Xu, X.-S., Griffin, W. L., O'Reilly, S. Y., & Xia, Q.-K. (2011). H2O contents and their modification in the Cenozoic subcontinental lithospheric mantle beneath the Cathaysia block, SE China. *Lithos*, *126*(3-4), 182–197.

Zhang, B., & Yoshino, T. (2017). Effect of graphite on the electrical conductivity of the lithospheric mantle. *Geochemistry, Geophysics, Geosystems*, *18*(1), 23–40.

Zlotnik, S., Afonso, J. C., Díez, P., & Fernández, M. (2008). Small-scale gravitational instabilities under the oceans: Implications for the evolution of oceanic lithosphere and its expression in geophysical observables. *Philosophical magazine*, *88*(28-29), 3197–3217.